1 **The Education and Research 3D Radiative Transfer Toolbox (EaR³T) – Towards the**
2 **Mitigation of 3D Bias in Airborne and Spaceborne Passive Imagery Cloud Retrievals**

4 Hong Chen[1,2], K. Sebastian Schmidt[1,2], Steven T. Massie[2], Vikas Nataraja[2], Matthew S. Norgren[2],
5 Jake J. Gristey[3,4], Graham Feingold[4], Robert E. Holz[5], Hironobu Iwabuchi[6]
6

8 [1]Department of Atmospheric and Oceanic Sciences, University of Colorado, Boulder, CO, USA
9 [2]Laboratory for Atmospheric and Space Physics, University of Colorado, Boulder, CO, USA
10 [3]Cooperative Institute for Research in Environmental Sciences, University of Colorado,
11 Boulder, CO, USA
12 [4]NOAA Chemical Sciences Laboratory, Boulder, CO, USA
13 [5]Space Science and Engineering Center, University of Wisconsin–Madison, Madison, WI, USA
14 [6]Center for Atmospheric and Oceanic Studies, Tohoku University, Sendai, Miyagi, Japan
15
16
17
18
19 *Correspondence to*: Hong Chen (hong.chen-1@colorado.edu)

20 **Abstract**

21   We introduce the Education and Research 3D Radiative Transfer Toolbox (EaR^{3}T) for quantifying

22 and mitigating artifacts in atmospheric radiation science algorithms due to spatially inhomogeneous clouds

23 and surfaces, and show the benefits of automated, realistic radiance and irradiance generation along

24 extended satellite orbits, flight tracks from entire aircraft field missions, and synthetic data generation from

25 model data. EaR^{3}T is a modularized Python package that provides high-level interfaces to automate the

26 process of 3D radiative transfer (RT) calculations. After introducing the package, we present initial findings

27 from four applications, which are intended as blueprints to future in-depth scientific studies. The first two

28 applications use EaR^{3}T as a satellite radiance simulator for the NASA Orbiting Carbon Observatory 2

29 (OCO-2) and Moderate Resolution Imaging Spectroradiometer (MODIS) missions, which generate

30 synthetic satellite observations with 3D-RT on the basis of cloud field properties from imagery-based

31 retrievals and other input data. In the case of inhomogeneous cloud fields, we show that the synthetic

32 radiances are often inconsistent with the original radiance measurements. This lack of radiance consistency

33 points to biases in heritage imagery cloud retrievals due to sub-pixel resolution clouds and 3D-RT effects.

34 They come to light because the simulator's 3D-RT engine replicates processes in nature that conventional

35 1D-RT retrievals do not capture. We argue that 3D radiance consistency (closure) can serve as a metric for

36 assessing the performance of a cloud retrieval in presence of spatial cloud inhomogeneity even with limited

37 independent validation data. The other two applications show how airborne measured irradiance data can

38 be used to independently validate imagery-derived cloud products via radiative closure in irradiance. This

39 is accomplished by simulating downwelling irradiance from geostationary cloud retrievals of Advanced

40 Himawari Imager (AHI) along all the below-cloud aircraft flight tracks of the Cloud, Aerosol and Monsoon

41 Processes Philippines Experiment (CAMP^{2}Ex, NASA 2019), and comparing the irradiances with the

42 collocated airborne measurements. In contrast to isolated case studies in the past, EaR^{3}T facilitates the use

43 of observations from entire field campaigns for the statistical validation of satellite-derived irradiance. From

44 the CAMP^{2}Ex mission, we find a low bias of 10% in the satellite-derived cloud transmittance, which we

45 are able to attribute to a combination of the coarse resolution of the geostationary imager and 3D-RT biases.

46 Finally, we apply a recently developed context-aware Convolutional Neural Network (CNN) cloud retrieval

47 framework to high-resolution airborne imagery from CAMP^{2}Ex and show that the retrieved cloud optical

48 thickness fields lead to better 3D radiance consistency than the heritage independent pixel algorithm,

49 opening the door to future mitigation of 3D-RT cloud retrieval biases.

1. Introduction

Three-dimensional cloud effects in imagery-derived cloud properties have long been considered an unavoidable error source when estimating the radiative effect of clouds and aerosols. Consequently, research efforts involving satellite, aircraft, and surface observations in conjunction with modeled clouds and radiative transfer calculations have focused on systematic bias quantification under different atmospheric conditions. Barker and Liu (1995) studied the so-called independent pixel approximation (IPA) bias in cloud optical thickness (COT) retrievals from shortwave cloud reflectance. The bias arises when approximating the radiative transfer relating to COT and measured reflectance at the pixel or cloud column level through one-dimensional (1D) radiative transfer (RT) calculations, while ignoring its radiative context. However, net horizontal photon transport and other effects such as shading engender column-to-column radiative interactions that can only be captured in a three-dimensional (3D) framework, and can be regarded as a 3D perturbation or bias relative to the 1D-RT (IPA) baseline. 3D biases affect not only cloud remote sensing but they also propagate into the derived irradiance fields and cloud radiative effects (CRE). Since the derivation of regional and global CRE relies heavily on satellite imagery, any systematic 3D bias impacts the accuracy of the Earth's radiative budget. Likewise, imagery-based aerosol remote sensing in the vicinity of clouds can be biased by net horizontal photon transport (Marshak et al., 2008). Additionally, satellite shortwave spectroscopy retrievals of CO_2 mixing ratio are affected by nearby clouds (Massie et al., 2017), albeit through a different physical mechanism than in aerosol and cloud remote sensing (Schmidt et al., 2022).

Given the importance of 3D perturbations for atmospheric remote sensing, ongoing research seeks to mitigate the 3D effects. Cloud tomography, for example, inverts multi-angle radiances to infer the 3D cloud extinction distribution (Levis et al., 2020). This is achieved through iterative adjustments to the cloud field until the calculated radiances match the observations. Convolutional neural networks (CNNs, Masuda et al., 2019; Nataraja et al., 2022) account for 3D-RT perturbations in COT retrievals through pattern-based machine learning that operates on collections of imagery pixels, rather than treating them in isolation like IPA. Unlike tomography, CNNs require training based on extensive cloud-type specific synthetic data with the ground truth of cloud optical properties and their associated radiances from 3D-RT calculations. Once the CNNs are trained, they do not require real-time 3D-RT calculations and can therefore be useful in an operational setting. Whatever the future may hold for context-aware multi-pixel or multi-sensor

81   cloud retrievals, there is a paradigm shift on the horizon that started when the radiation concept

82   for the Earth Clouds, Aerosol and Radiation Explorer (EarthCARE, Illingworth et al., 2015) was

83   first proposed (Barker et al., 2012). It foresees a closure loop where broadband radiances, along

84   with irradiance, are calculated in a 3D-RT framework from multi-sensor input fields (Barker et al.,

85   2011), and subsequently compared to independent observations by radiometers pointing in three

86   directions (nadir, forward-, and backward-viewing along the orbit). This built-in radiance closure

87   can serve as an accuracy metric for any downstream radiation products such as heating rates and

88   CRE. Any inconsistencies can be used to nudge the input fields towards the truth in subsequent

89   loop iterations akin to optimal estimation, or propagated into uncertainties of the cloud and

90   radiation products.

91   This general approach to radiative closure is also being considered for the National

92   Aeronautics and Space Administration (NASA) Atmospheric Observation System (AOS,

93   developed under the A-CCP, Aerosol and Cloud, Convection and Precipitation study), a mission

94   that is currently in its early implementation stages. Owing to its focus on studying

95   aerosol-cloud-precipitation-radiation interactions at the process level, it requires radiation

96   observables at a finer spatial resolution than achieved with missions to date. At target scales close

97   to 1 km, 3D-RT effects are much more pronounced than at the traditional 20 km scale of NASA

98   radiation products (O'Hirok and Gautier, 2005; Ham et al., 2014; Song et al., 2016; Gristey et al.,

99   2020a). Since this leads to biases beyond the desired accuracy of the radiation products, mitigation

100   of 3D-RT cloud remote sensing biases needs to be actively pursued over the next few years.

101   Transitioning to an explicit treatment of 3D-RT in operational approaches entails a new

102   generation of code architectures that can be easily configured for various instrument constellations,

103   interlink remote sensing parameters with irradiances, heating rates, and other radiative effects, and

104   can be used for automated processing of large data quantities. A number of 3D solvers are available

105   for different purposes, for example, the I3RC (International Intercomparison of 3D Radiation

106   Codes: Cahalan et al., 2005) community Monte Carlo code[1], which now also includes an online

107   simulator[2] (Gatebe et al., 2021); MCARaTS (Monte Carlo Atmospheric Radiative Transfer

108   Simulator[3]: Iwabuchi, 2006); MYSTIC (Monte Carlo code for the physically correct tracing of

---

[1] https://earth.gsfc.nasa.gov/climate/model/i3rc, last accessed on 26 November, 2022.
[2] http://i3rcsimulator.umbc.edu, last accessed on 26 November, 2022.
[3] https://sites.google.com/site/mcarats/monte-carlo-atmospheric-radiative-transfer-simulator-mcarats, last accessed on 26 November, 2022.

photons in cloudy atmospheres: Mayer, 2009), which is embedded in libRadtran (library for radiative transfer, Mayer and Kylling, 2005); McSCIA (Monte Carlo [RT] for SCIAmachy: Spada et al., 2006), which is optimized for satellite radiance simulations (including limb-viewing) in a spherical atmosphere; McARTIM (Deutschmann et al., 2011), with several hyperspectral polarimetric applications such as differential optical absorption spectroscopy; and SHDOM (Spherical Harmonic Discrete Ordinate Method[4]: Evans, 1998), which, unlike the other methods, is a deterministic solver with polarimetric capabilities (Doicu et al., 2013; Emde et al., 2015) that is differentiable and can therefore be used for tomography (Loveridge et al., 2022).

For the future operational application of 3D-RT, it is, however, desirable to run various different solvers in one common architecture that automates the processing of various formats of 3D atmospheric input fields (including satellite data), allows the user to choose from various options for atmospheric absorption and scattering, and simulates radiance and irradiance data for real-world scenes. Here, we introduce one such tool that could serve as the seed for this architecture: the Education and Research 3D Radiative Transfer Toolbox (EaR^{3}T). It has been developed over the past few years at the University of Colorado to automate 3D-RT calculations based on imagery or model cloud fields with minimal user input. EaR^{3}T is maintained and extended by graduate students as part of their education, and applied to various different research projects including machine learning for atmospheric radiation and remote sensing (Gristey et al., 2020b; 2022; Nataraja et al., 2022), as well as radiative closure and satellite simulators (this paper and Schmidt et al., 2022). It is implemented as a modularized Python package with various application codes that combine the functionality in different ways, which, once set up, autonomously process large amounts of data required by airborne and satellite remote sensing and for machine learning applications.

The goal of the paper is to introduce EaR^{3}T as a versatile tool for systematically quantifying and mitigating 3D cloud effects in radiation science as foreseen in future missions. To do so, we will first showcase EaR^{3}T as an automated radiance simulator for two satellite instruments, the Orbiting Carbon Observatory-2 (OCO-2, this application is referred to as App. 1 in this manuscript) and the Moderate Resolution Imaging Spectroradiometer (MODIS, application code 2, App. 2) from publicly available satellite retrieval products. In the spirit of radiance closure, the intended use is the comparison of modeled radiances with the original measurements to assess the accuracy

---

[4] https://coloradolinux.com/shdom, last accessed on 26 November, 2022.

142 of the input data, as follows: operational IPA COT products are made using 1D-RT, and thus the

143 accompanying radiances are consistent with the original measurements under that 1D-RT

144 assumption only. That is, self-consistency is assured if 1D-RT is used in both the inversion and

145 radiance simulation. However, since nature creates 3D-RT radiation fields, we break this

146 traditional symmetry in this manuscript and introduce the concept of 3D radiance consistency

147 where closure is only achieved if the original measurements are consistent with the 3D-RT (rather

148 than the 1D-RT) simulations. The level of inconsistency is then used as a metric for the magnitude

149 of 3D-RT retrieval artifacts as envisioned by the architects of the EarthCARE radiation concept

150 (Barker et al., 2012).

151 Subsequently, we discuss applications where EaR^{3}T performs radiative closure in the

152 traditional sense, i.e., between irradiances derived from satellite products and collocated airborne

153 or ground-based observations. The aircraft Cloud, Aerosol and Monsoon Processes Philippines

154 Experiment (CAMP^{2}Ex, Reid et al., 2022), conducted by NASA in the Philippines in 2019, serves

155 as a testbed of this approach. Here, we use EaR^{3}T's automated processing capabilities to derive

156 irradiance from geostationary imagery cloud products and then compare these to cumulative

157 measurements made along all flight legs of the campaign (application code 3, App. 3). In contrast

158 to previous studies that often rely on a number of cases (e.g., Schmidt et al., 2010; Kindel et al.,

159 2010), we perform closure systematically for the entire data set, enabling us to identify 3D-RT

160 biases in a statistically significant manner. Finally, we apply a regionally and cloud type specific

161 CNN, introduced by Nataraja et al. (2022) that is included with the EaR^{3}T distribution, to high-

162 resolution camera imagery from CAMP^{2}Ex. This last example demonstrates mitigation of 3D-RT

163 biases in cloud retrievals using the concept of radiance closure to quantify its performance against

164 the baseline IPA (application code 4).

165 The general concept of EaR^{3}T with an overview of the applications, along with the data

166 used for both parts of the paper is presented in section 2, followed by a description of the

167 procedures of EaR^{3}T in section 3. Results for the OCO-2 and MODIS satellite simulators (part 1)

168 are shown in section 4, followed by the quantification and mitigation of 3D-RT biases with

169 CAMP^{2}Ex data in section 5 and section 6 (part 2). A summary and conclusion are provided in

170 section 7. The code, along with the applications presented in this paper, can be downloaded from

171 the GitHub repository: https://github.com/hong-chen/er3t.

172

2. Functionality and Data Flow within EaR³T

2.1 Overview

177

178

179   To introduce EaR³T as a satellite radiance simulator tool and to demonstrate its use for the

180   quantification and mitigation of 3D cloud remote sensing biases, five applications (Figure 1) are

181   included in the GitHub software release, four of which are discussed in this paper:

182

183
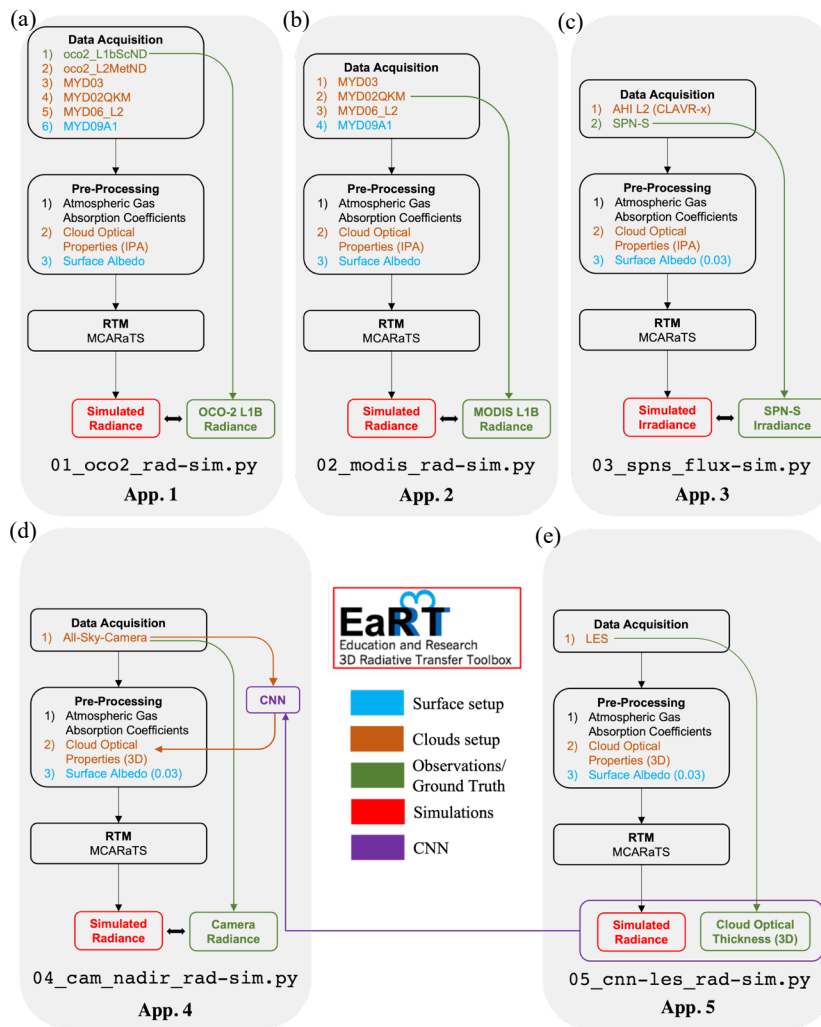
Figure 1. Flow charts of EaR³T applications for (a) OCO-2 radiance simulation at 768.52 nm (data described in section 2.2.1 and 2.2.2, results discussed in section 4), (b) MODIS radiance simulation at 650 nm (data described in section 2.2.1, results discussed in section 4), (c) SPN-S irradiance simulation at 745 nm (data described in section 2.2.3 and 2.2.4, results discussed in section 5), (d) all-sky camera radiance simulation at 600 nm (data described in section 2.2.5, results discussed in section 6), and (e) radiance simulation at 600 nm based on LES data for CNN training (Appendix B). The data products and their abbreviations are described in section 2.2.

| | Deleted: not included in this paper |

1. App. 1, section 4.1 (`examples/01_oco2_rad-sim.py`): Radiance simulations along the track of OCO-2, based on data products from MODIS and others – to assess consistency (closure) between simulated and measured radiance;

| | Deleted: APP |
| | Deleted: |

2. App. 2, section 4.2 (`examples/02_modis_rad-sim.py`): MODIS radiance simulations – to assess self-consistency of MODIS level-2 (L2) products with the associated radiance fields (L1B product) under spatially inhomogeneous conditions;

| | Deleted: APP |

3. App. 3, section 5 (`examples/03_spns_flux-sim.py`): Irradiance simulations along aircraft flight tracks, utilizing the L2 cloud products of the AHI, and comparison with aircraft measurements – to quantify retrieval biases due to 3D cloud structure based with data from an entire aircraft field campaign;

| | Deleted: APP |
| | Deleted: |

4. App. 4, section 6 (`examples/04_cam_nadir_rad-sim.py`): Mitigation of 3D cloud biases in passive imagery COT retrievals from an airborne camera, application of a convolutional neural network (CNN) and subsequent comparison of CNN-derived radiances with the original measurements – to illustrate how the radiance self-consistency concept assesses the fidelity of cloud retrievals.

| | Deleted: APP |

5. App. 5, Appendix B (`examples/05_cnn-les_rad-sim.py`): Generation of training data for the CNN (App. 4) based on LES inputs. The training datasets contains 1) the ground truth of COT from the LES data; 2) realistic radiance simulated by EaR³T based on the LES cloud fields.

Figure 1 shows the high-level workflow of the applications. The first four share the general concept of evaluating simulations (the output from the EaR³T, indicated in red at the bottom of each column) with observations (indicated in green at the bottom) from various satellite and aircraft instruments. The results for the first four applications are interpreted in section 4.1, section 4.2, section 5, and section 6. The results for App. 5 are discussed in detail in a separate paper by

Nataraja et al. (2022). In this paper, we will only provide a brief description for App. 5 in Appendix B. The workflow of each application consists of three parts – 1) data acquisition, 2) pre-processing, and 3) RTM setup and execution. EaR³T includes functions to ingest data from various different sources, e.g., satellite data from publicly available data archives, which can be combined in different ways to accommodate input data depending on the application specifics. For example, in App. 1, EaR³T is used to automatically download and process MODIS and OCO-2 data files based on the user-specified region, date and time. Building on the templates provided in the current code distribution, the functionality can be extended to new spaceborne or airborne instruments. The fifth column of Figure 1 shows an application that differs from the first four, and was developed for earlier papers (Gristey et al., 2020a and 2020b; Nataraja et al., 2022; Gristey et al., 2022). In contrast to the first four, which use imagery products as input, the fifth application ingests model output from a Large Eddy Simulation (LES) and produces irradiance data for surface energy budget applications, or synthetic radiance fields for training a CNN. Details and results are described in the respective papers. Furthermore, Schmidt et al. (2022) builds upon App. 1 to study the mechanism of 3D cloud biases in OCO-2 passive spectroscopy retrievals.

After the required data files have been downloaded in the data acquisition step, EaR³T pre-processes them and generates the optical properties of atmospheric gases, clouds, aerosols, and the surface. In Figure 1, the mapping from input data to these properties is color-coded component-wise (brown for associated cloud property processing if available, blue for associated surface property processing if available, green for associated ground truth property). The version used in this paper (v0.1.0; Chen and Schmidt, 2022) only includes MCARaTS as the 3D RT solver, but others are planned for the future. MCARaTS is a radiative transfer solver uses Monte Carlo photon-tracing method (Iwabuchi, 2006). It outputs radiation (radiance or irradiance) based on the inputs of radiative properties of surface and atmospheric constituents (e.g., gases, aerosols, clouds) such as single scattering albedo, scattering phase function, or asymmetry parameters, along with solar and sensor viewing geometries. The setup of these input properties is implemented in EaR³T's pre-processing steps, which translates atmospheric properties into solver-specific input with minimum user intervention. To achieve this, EaR³T is modular so that it can be extended as new solvers are added. Although the five specific applications in this paper do not include aerosol layers, the setup of aerosol fields is fully supported and has been used in other applications (e.g., Gristey et al., 2022). After pre-processing, the optical properties are fed into the RT solver. Finally,

Deleted: APP

Deleted: APP

Deleted: -

Deleted: -

Deleted: Although the

Deleted: current

Deleted: the Monte Carlo Atmospheric Radiative Transfer Simulator (…

Deleted: , Iwabuchi, 2006)

Deleted: ,

265 the user obtains radiation output from EaR^{3}T, either radiance or irradiance. The output is saved in
266 HDF5 format and can be easily distributed and accessed by various programming languages. The
267 data variables contained in the HDF5 output are provided in Table 1.
268

Metadata			
Variable Name	Description	Data Type	Dimension
mean/N_photon	Number of photons per run	Array	N_g
mean/N_run	Number of runs	Integer value	N/A
mean/toa	TOA downwelling flux	Float value	N/A
Radiance			
Variable Name	Description	Data Type	Dimension
mean/rad	Radiance field at user specified altitude averaged over different runs	Array	(N_x, N_y)
mean/rad_std	Standard deviation of the radiance fields from different runs	Array	(N_x, N_y)
Irradiance			
Variable Name	Description	Data Type	Dimension
mean/f_down	Downwelling irradiance averaged over different runs	Array	(N_x, N_y, N_z)
mean/f_down_std	Standard deviation of the downwelling irradiance from different runs	Array	(N_x, N_y, N_z)
mean/f_down_diffuse	Diffuse downwelling irradiance averaged over different runs	Array	(N_x, N_y, N_z)
mean/f_down_diffuse_std	Standard deviation of the diffuse downwelling irradiance from different runs	Array	(N_x, N_y, N_z)

mean/f_down_direct	Direct downwelling irradiance averaged over different runs	Array	(N_x, N_y, N_z)
mean/f_down_direct_std	Standard deviation of the direct downwelling irradiance from different runs	Array	(N_x, N_y, N_z)
mean/f_up	Upwelling irradiance averaged over different runs	Array	(N_x, N_y, N_z)
mean/f_up_std	Standard deviation of the upwelling irradiance from different runs	Array	(N_x, N_y, N_z)

269

270 **Table 1**: Data variables contained in the output HDF5 file from EaR^{3}T for radiance and irradiance calculations. The
271   radiance is simulated with a user-specified sensor geometry at a given altitude using forward photon tracing.
272   The data variables listed under Metadata are included for both radiance and irradiance calculations. N_x,
273   N_y, and N_z are the number of pixels along x, y, and z direction, respectively. N_g is the number of g,
274   explained in section 3 – Correlated-k.

275

276   The aforementioned three steps – data acquisition, pre-processing, and RTM setup and
277 execution are automated such that the 3D/1D-RT calculations can be performed for any region at
278 any date and time using satellite or aircraft data or other data resources such as LES. EaR^{3}T is
279 hosted on GitHub at https://www.github.com/hong-chen/er3t. Since it is developed as an
280 educational and research 3D-RT tool collection by students, it is a living code base, intended to be
281 updated over time. The master code modules for the five applications as listed in Figure 1 are
282 included in the EaR^{3}T package under the examples directory. In the current release (v0.1.0),
283 only a limited documentation for the installation and usage, including example codes for EaR^{3}T,
284 are provided. More effort will be dedicated for documentation in the near-future.

285

286 **2.2 Data**

287   The radiance simulations in App. 1 and App. 2 use data from the OCO-2 and MODIS-Aqua
288 instruments, both of which are in a sun-synchronous polar orbit with an early-afternoon equator
289 crossing time within NASA's A-Train satellite constellation. Figure 2 visualizes radiance
290 measurements by OCO-2 in the context of MODIS Aqua imagery over a partially vegetated and

297   partially cloud-covered land, illustrating that MODIS provides imagery and scene context for

298   OCO-2, which in turn observes radiances from a narrow swath. The region is located in southwest

299   Colorado in the United States of America. We selected this case because both the surface and

300   clouds are varied along with diverse surface types. The surface features green forest and brown

301   soil, whereas clouds include small cumulus and large cumulonimbus. In addition, this scene

302   contains relatively homogeneous cloud fields in the north and inhomogeneous cloud fields in the

303   south, which allows us to evaluate the simulations from various aspects of cloud morphology. To

304   simulate the radiances of both instruments we use data products from OCO-2 and MODIS, as well

305   as reanalysis products from NASA's Global Modeling and Assimilation Office (GMAO) sampled

306   at OCO-2 footprints and distributed along with OCO-2 data (section 2.2.2).

307
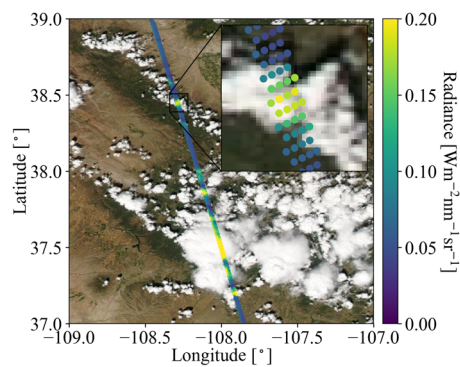
308

309   **Figure 2**. OCO-2 measured radiance (units: $Wm^{-2}nm^{-1}sr^{-1}$) at 768.52 nm, overlaid on MODIS Aqua RGB imagery

310   over southwestern Colorado (USA) on 2 September, 2019. The inset shows an enlarged portion along the

311   track, illustrating that OCO-2 radiances co-vary with MODIS-Aqua radiance observations.

312

313   For App. 3 (irradiance simulations and 3D cloud bias quantification), we use geostationary

314   imagery from the Japanese Space Agency's Advanced Himawari Imager to provide cloud

315   information in the area of the flight path of the NASA CAMP²Ex aircraft (Reid et al., 2022). The

316   AHI data are used in conjunction with aircraft measurements of shortwave spectral radiation

317   (section 2.2.4). Subsequently (App. 4: 3D cloud bias mitigation), we demonstrate the concept of

318   radiance closure under partially cloudy conditions with airborne camera imagery (section 2.2.5).

319   The underlying cloud retrieval is based on a convolutional neural network (CNN), which is

Deleted: APP

Deleted: APP

322 described in a related paper (Nataraja et al., 2022) in this special issue and relies on EaR³T-
323 generated synthetic radiance data based on Large Eddy Simulations (LES).
324
2.2.1 Moderate Resolution Imaging Spectroradiometer (MODIS)

326   The MODIS instruments are multi-use multispectral radiometers onboard NASA's Terra
327 and Aqua satellites, which were launched in 1999 and 2002 respectively. MODIS was conceived
328 as a central element of the Earth Observing System (EOS, King and Platnick, 2018). For App. 1
329 and App. 2, EaR³T ingests MODIS level 1B radiance products at the quarter kilometer scale
330 (channels 1 and 2, bands centered at 650 and 860 nm), MxD02QKM, where 'x' stands for 'O' in
331 the case of MODIS on Terra, and 'Y' in the case of Aqua data), the geolocation product (MxD03),
332 the level 2 cloud product (MxD06), and the surface reflectance product (MxD09A1). For this paper,
333 we use only Aqua data (MYD), from data collection 6.1. All the data are publicly available, and
334 are distributed at the LAADS (Level-1 and Atmosphere Archive & Distribution System)
335 Distributed Active Archive Center (DAAC) by NASA's Goddard Space Flight Center.

336   For cloud properties in App. 2, we use the MODIS cloud product (MxD06L2, collection
337 6.1). It provides cloud properties such as cloud optical thickness (COT), cloud effective radius
338 (CER), cloud thermodynamic phase, cloud top height (CTH), etc. (Nakajima and King, 1990;
339 Platnick et al., 2003). Since 3D cloud effects such as horizontal photon transport are most
340 significant at small spatial scales (e.g., Song et al., 2016), we use the high-resolution red (650 nm)
341 channel 1 (250 m), and derive COT directly from the reflectance in the Level-1B data
342 (MYD02QKM) instead of using the coarser-scale operational product from MYD06. CER and
343 CTH are sourced from MYD06 and re-gridded to 250 m. The EaR³T strategy for MODIS data is
344 similar, in principle, to the more advanced method by Deneke et al. (2021), which uses a
345 high-resolution wide-band visible channel from geostationary imagery to up-sample narrow-band
346 coarse-resolution channels. However, we simplified cloud detection and derivation of COT from
347 reflectance data for the purpose of our paper by using a threshold method (Appendix C1) and the
348 two-stream approximation (Appendix C2). In future versions of EaR³T this will be upgraded to
349 more sophisticated algorithms. A simple algorithm (Appendix D1) is used to correct for the
350 parallax shift based on the sensor geometries and cloud heights. The cloud top height data is
351 provided by the MODIS L2 cloud product and assuming cloud base is the same.

Deleted: is currently flying
Deleted: on
Deleted: They
Deleted: The
Deleted: are
Deleted: is
Deleted: multi-use multispectral radiometers
Deleted: s
Deleted: APP
Deleted: APP
Deleted: (
Deleted: APP
Deleted: -
Deleted: A1
Deleted: A2
Deleted: B1

368   For the surface albedo required by the RTM, we used MYD09A1, which provides
369 cloud-cleared surface reflectance observations aggregated over an 8-day period (Vermote et al.,
370 2015). This product is available on a sinusoidal grid with a spatial resolution of 500 m for MODIS
371 band 2, and includes atmospheric correction for gas and aerosol scattering and absorption.
372 Assuming a Lambertian surface in this first release of EaR^{3}T, we used surface reflectance as
373 surface albedo input to the RTM.
374

2.2.2 Orbiting Carbon Observatory 2 (OCO-2)

376   The OCO-2 satellite was inserted into NASA's A-Train constellation in 2014 and flies
377 about 6 minutes ahead of Aqua. OCO-2 provides the column-averaged carbon dioxide (CO_2)
378 dry-air mole fraction (XCO_2) through passive spectroscopy based on hyperspectral radiance
379 observations in three narrow wavelength regions, the Oxygen A-Band (~0.76 micron), the weak
380 CO_2 band (~1.60 micron), and the strong CO_2 band (~2.06 micron). As shown in the inset of Figure
381 2, it takes measurements in eight footprints across a narrow swath. Each of the footprints has a
382 size around 1-2 km, and the spectra for the three bands are provided by separate, co-registered
383 spectrometers (Crisp et al., 2015).
384   The OCO-2 data products of 1) Level 1B calibrated and geolocated science radiance
385 spectra (L1bScND), 2) standard Level 2 geolocated XCO_2 retrievals results (L2StdND), 3)
386 meteorological parameters interpolated from GMAO (L2MetND) at OCO-2 footprint location are
387 downloaded from NASA GES DISC (Goddard Earth Science Data Archive and Information
388 Services Center) data archive (https://oco2.gesdisc.eosdis.nasa.gov/data/OCO2_DATA). Since
389 MODIS on Aqua overflies a scene 6 minutes after OCO-2, the clouds move with the wind over
390 this time period. We therefore added a wind correction on top of the parallax-corrected cloud fields
391 obtained from MODIS (section 2.2.1). This was done with the 10 m wind speed data from
392 L2MetND (see Appendix D2). For the same scene as shown in Figure 2, Figure 3 shows (a) COT,
393 (b) CER, and (c) CTH, all corrected for both parallax and wind effects (these corrections are shown
394 in Figure A2 in Appendix D). The parallax and wind corrections are imperfect as certain
395 assumptions are involved. For example, they rely on the cloud top height from the MODIS cloud
396 product. In addition, they process the whole scene with one single sensor viewing geometry. To
397 minimize artifacts introduced by the assumptions, one can apply the simulation to a smaller region.
398

| Deleted: reflectance, we used |
| Deleted: for |
| Deleted: - |
| Deleted: are |
| Deleted: - |
| Deleted: B2 |
| Deleted: effect |
| Deleted: A1 |
| Deleted: B |

408

409
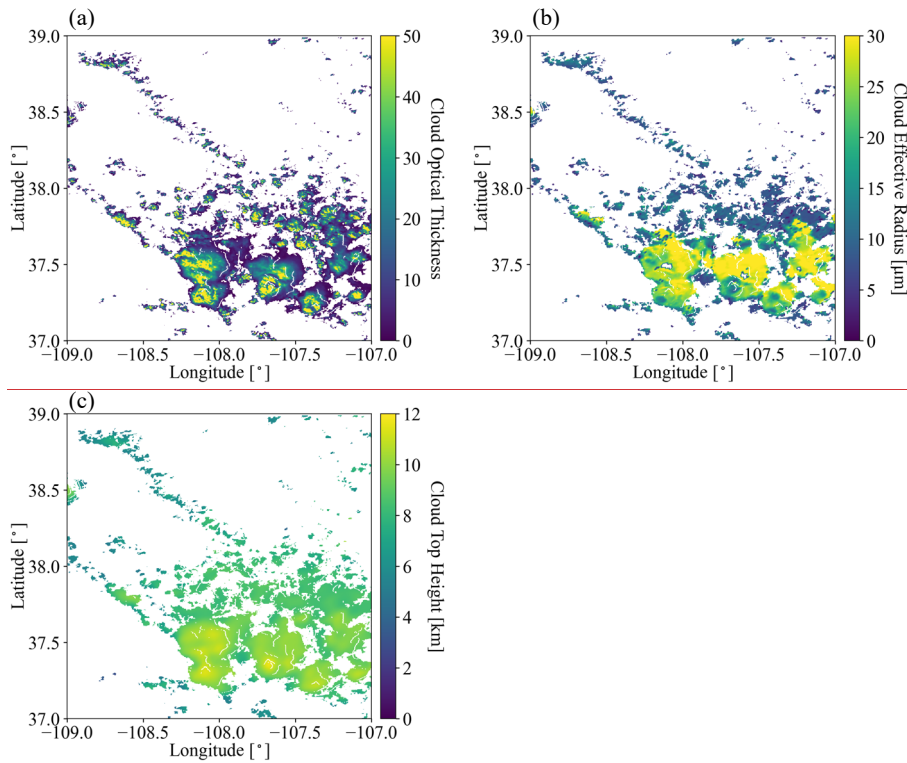
410

411 **Figure 3**. **(a)** Cloud optical thickness derived from MODIS L1B radiance at 650 nm by the two-stream approximation
412 (Eq. A2), **(b)** cloud effective radius (units: μm), and **(c)** cloud top height (units: km) collocated from the
413 MODIS L2 cloud product. The locations of the cloudy pixels were shifted to account for parallax and wind
414 effects. The parallax correction ranged from near 0 for low clouds and 1 km for high clouds (10 km CTH).
415 The wind correction was around 0.8 km, given the average wind speed of 2 m/s to the east.

416

417   The OCO-2 data (L2StdND) themselves only provide sparse surface reflectance for the
418 footprints that are clear, while EaR^{3}T requires surface albedo for the whole domain. Therefore, we
419 used MYD09A1 as a starting point. However, since MODIS does not have a channel in the Oxygen
420 A-Band, MODIS band 2 (860 nm) was used as a proxy for the 760 nm OCO-2 channel as follows:
421 we collocated the OCO-2 retrieved 760 nm surface reflectance R_{OCO} within the corresponding 860
422 nm MODIS MYD09A1 data R_{MOD} as shown in Figure 4a (same domain as Figures 2 and 3) and

423 calculated a scaling factor assuming a linear relationship between R_{OCO} and R_{MOD} ($R_{OCO} = a \cdot R_{MOD}$).

424 Figure 4b shows R_{OCO} versus R_{MOD} for all cloud-free OCO-2 footprints. The red line shows a linear

425 regression (derived scale factor $a=0.93$). Optionally, the OCO-2-scaled MODIS-derived surface

426 reflectance fields can be replaced by the OCO-2 surface reflectance products for pixels where they

427 are available. The scaled surface reflectance is then treated as surface albedo input to the RTM

428 assuming a Lambertian surface.

429
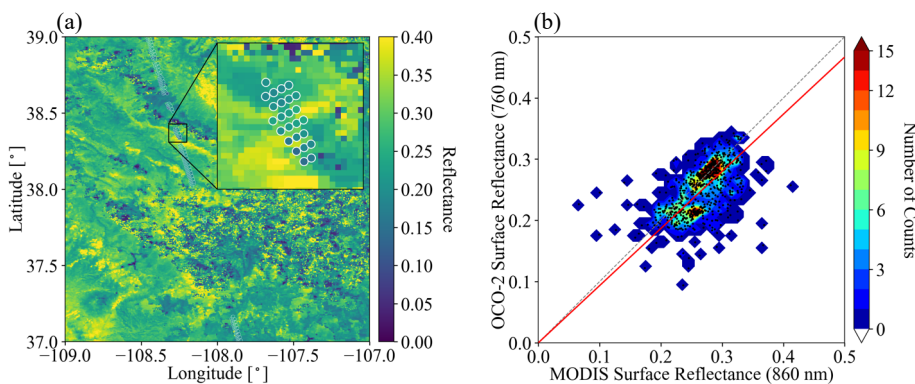
431 **Figure 4**. **(a)** Surface reflectance from the OCO-2 L2 product in the Oxygen A-band (near 760 nm), overlaid on the

432 surface reflectance from the MODIS MYD09 product at 860 nm. **(b)** OCO-2 surface reflectance at 760 nm

433 versus MODIS surface reflectance at 860 nm, along with linear regression ($y=ax$) as indicated by the red

434 line (slope $a=0.9337$).

435

436 **2.2.3 Advanced Himawari Imager (AHI)**

437 The Advanced Himawari Imager (AHI, used for App. 3) is a payload on Himawari-8, a

438 geostationary satellite operated by the Meteorological Satellite Center (MSC) of the Japanese

439 Meteorological Agency. The AHI provides 16 channels of spectral radiance measurements from

440 the shortwave (0.47μm) to the infrared (13.3μm). During CAMP²Ex, the NASA in-field

441 operational team closely collaborated with the team from MSC to provide AHI satellite imagery

442 at the highest resolution over the Philippine Sea. From the AHI imagery, the cloud product

443 generation system - Clouds from AVHRR Extended System (CLAVR-x), was used to generate

444 cloud products from the AHI imagery (Heidinger et al., 2014). The cloud products from CLAVR-

445 x include cloud optical thickness, cloud effective radius, and cloud top height at 2 (at nadir) to 5

449 km spatial resolution. Since AHI provides continuous regional scans every 10 minutes the AHI
450 cloud product has a temporal resolution of 10 minutes.
451
452 **2.2.4 Spectral Sunshine Pyranometer (SPN-S)**
453   The SPN-S is a prototype spectral version of the commercially available global-diffuse
454 SPN1 pyranometer (Wood et al., 2017; Norgren et al., 2022). The radiometer uses a 7-detector
455 design in combination with a fixed shadow mask that enables the simultaneous measurement of
456 both diffuse and global irradiances, from which the direct component of the global irradiance is
457 calculated via subtraction. The detector measures spectral irradiance from 350 to 1000 nm, and the
458 spectrum is sampled at 1 nm resolution with 1 Hz timing.
459   During the CAMP^{2}Ex mission, the SPN-S was mounted to the top of the NASA P-3 aircraft
460 where it sampled downwelling solar irradiance. To ensure accurate measurements, pre- and post-
461 mission laboratory-based calibrations were completed using tungsten "FEL" lamps that are
462 traceable to a National Institute of Standards and Technology standard. Additionally, the direct
463 and global irradiances were corrected for deviations of the SPN-S sensor plane from horizontal
464 that are the result of changes in the aircraft's pitch or roll. This attitude correction applied to the
465 irradiance data is a modified version of the method outlined in Long et al. (2010). However,
466 whereas Long et al. (2010) employ a "box" flight pattern to characterize the sensor offset angles,
467 in this study an aggregation of flight data containing aircraft heading changes under clear-sky
468 conditions are used as a substitute. The estimated uncertainty of the SPN-S system is 6 to 8%, with
469 4 to 6% uncertainty stemming from the radiometric lamp calibration process, and up to another 2%
470 resulting from insufficient knowledge of the sensor cosine response. The stability of the system
471 under operating conditions is 0.5%. A thorough description of the SPN-S and its calibration and
472 correction procedures is provided in Norgren et al. (2022). In this paper (App. 3) only the global
473 downwelling irradiance sampled by the 745 nm channel is used.
474
475 **2.2.5 Airborne All-Sky Camera (ASC)**
476   The All-Sky Camera (used for App. 4) is a commercially available camera (ALCOR
477 ALPHEA 6.0CW[5]) with fish-eye optics for hemispheric imaging. It has a Charge-Coupled Device

[5]https://www.alcor-system.com/common/allSky/docs/ALPHEA_Camera%20ALL%20SKY%20CAMERA_Doc.pdf last accessed on April 24, 2022.

Deleted: is

Deleted: APP

Deleted: APP

481 (CCD) detector that measures radiances in red, green, and blue channels. Radiometric and

482 geometric calibrations were performed at the Laboratory of Atmospheric and Space Physics at the

483 University of Colorado Boulder. The three-color channels are centered at 493, 555, and 626 nm

484 for blue, green, and red, respectively, with bandwidths of 50 – 100 nm. Only radiance data from

485 the red channel are used in this paper. The spatial resolution of the ASC depends on the altitude of

486 the aircraft and the viewing zenith angle. Across the hemispheric field of view of the camera, the

487 resolution of the field angle is approximately constant, at about 0.09º. At a flight level of 5 km,

488 this translates to a spatial resolution of 8 m at nadir. However, due to accuracy limitations of the

489 geometric calibration and the navigational data from Inertial Navigation System (INS), the nadir

490 geolocation accuracy could only be verified to within ±50 m. During the CAMP^{2}Ex flights, the

491 camera exposure time was set manually to minimize saturation of the detector. The standard image

492 frame rate is 1 Hz. The precision of the camera radiances is on the order of 1%, and the radiometric

493 accuracy is 6 – 7%.

494

495 **3. EaR^{3}T Procedures**

496 In the previous section, we described the general workflow of EaR^{3}T applications, along

497 with relevant data. In this section, we will focus on the specific implementation of the workflow

498 through the EaR^{3}T software package. It is a toolbox for 3D-RT with modules for automatic input

499 data download and processing, generation of radiative and optical properties of surface,

500 atmospheric gases, clouds and aerosols, wrappers for 3D-RT solvers and output post-processing,

501 with the end goal to simulate radiances and irradiances along entire satellite orbits or aircraft flight

502 tracks. Unlike established radiative transfer packages such as libRadtran (Mayer and Kylling, 2005;

503 Emde et al., 2016), which provide extensive libraries of optical properties along with a selection

504 of solvers, EaR^{3}T focuses on automated radiative transfer for two- or three-dimensional cloud,

505 aerosol, and surface input data, and therefore only comes with minimal options for optical

506 properties, and solvers. The initial release (version 0.1.0) is available at https://github.com/hong-

507 chen/er3t.

508 We will now walk through the OCO-2 and MODIS simulator applications with the codes

509 `examples/01_oco2_rad-sim.py` (App. 1) and `examples/02_modis_rad-sim.py`

510 (App. 2). The data acquisition (first step in Figure 1) uses functions in `er3t/util`. App. 1 and

515 App. 2 use the functions in `er3t/util/modis.py` and `er3t/util/oco2.py` for

516 downloading the MODIS and OCO-2 data files from the respective NASA data archives and for

517 processing the data (e.g., geo-mapping, gridding etc.). The user supplies minimum input (date and

518 time, as well as latitudes and longitudes of the region of interest), which need to be specified in

519 `download_modis_https` and `download_oco2_https` (from `er3t/util`). For

520 example, for App. 1 and App. 2, the only user inputs are the date and time and the region of interest

521 – in this case September 2, 2019, with the westernmost, easternmost, southernmost, and

522 northernmost longitudes and latitudes of 109°W, 107°W, 37°N, and 39°N. In order for EaR³T to

523 access any data archives such as NASA Earthdata, the user needs to create an account with them

524 and store the credentials locally (detailed instructions are provided separately along with the EaR³T

525 distribution).

526   After the data acquisition step, the satellite data are fed into the pre-processing step for 1)

527 atmospheric gases (`er3t/pre/atm`), 2) clouds (`er3t/pre/cld`), 3) surface

528 (`er3t/pre/sfc`) as shown in Figure 1. In the default configuration of the App. 1, the standard

529 US atmosphere (Anderson et al., 1986; included in the EaR³T repository) is used within `atm`.

530 EaR³T supports the input of user-specified atmospheric profiles, e.g., atmospheric profiles from

531 reanalysis data for App. 2 as described in Schmidt et al. (2022), by making changes in

532 `atm_atmmod` (from `er3t/pre/atm`). Subsequently, molecular scattering coefficients are

533 calculated by `cal_mol_ext` (from `er3t/util`), and absorption coefficients for atmospheric

534 gases are generated by (`er3t/pre/abs`). At the current development stage, two options are

535 available:

536 1. Line-by-line (used by App. 1): The repository includes a sample file of absorption coefficient

537 profiles for a subset of wavelengths within OCO-2's Oxygen A-Band channel, corresponding

538 to a range of atmospheric transmittance values from low (opaque) to high (so-

539 called "continuum" wavelength). They were generated by an external code (Schmidt et al.,

540 2022) based on OCO-2's line-by-line absorption coefficient database (ABSCO, Payne et al.,

541 2020). For each OCO-2 spectrometer wavelength within a given channel, hundreds of

542 individual absorption coefficient profiles at the native resolution of ABSCO need to be

543 considered across the instrument line shape (ILS, also known as the slit function) of the

544 spectrometer. The ILS, as well as the incident solar irradiance, are also included in the file.

545 In subsequent steps, EaR³T performs RT calculations at the native spectral resolution of

557 ABSCO, but then combines the output by convolving with the ILS and outputs OCO-2
558 radiances or reflectances at the subset of wavelengths. For probabilistic (Monte Carlo) RT
559 solvers such as MCARaTS, the number of photons can be kept relatively low (e.g., 10^6
560 photons), and can be adjusted according to the values of the ILS at a particular ABSCO
561 wavelength. Any uncertainty at the ABSCO spectral resolution due to photon noise is greatly
562 reduced by convolving with the ILS for the final output.

563 2. Correlated-k (used by App. 2): This approach (Mlawer et al., 1997) is appropriate for
564 instruments such as MODIS with much coarser spectral resolution than OCO-2, as well as
565 for broadband calculations. In contrast to the line-by-line approach, RT calculations are not
566 performed at the native resolution of the absorption database, but at Gaussian quadrature
567 points (called "g's") that represent the full range of sorted absorption coefficients, and then
568 combined using Gaussian quadrature weights. The repository includes an absorption
569 database from Coddington et al. (2008), developed specifically for a radiometer with
570 moderate spectral resolution on the basis of HITRAN (high-resolution transmission
571 molecular absorption database) 2004 (Rothman et al., 2005). It was created for the ILS of
572 the airborne Solar Spectral Flux Radiometer (SSFR, Pilewski et al., 2003), but is applied to
573 MODIS here, which has a moderate spectral resolution of 8-12 nm with 20-50 nm
574 bandwidths. It uses 16 absorption coefficient bins (g's) per target wavelength (this could
575 either be an individual SSFR or a MODIS channel), which are calculated by EaR^{3}T with the
576 Coddington et al. (2008) database using the mixing ratios of atmospheric gases in the
577 previously ingested profile. In future implementations, the code will be updated to enable
578 flexible ILS and broadband calculations.

579 The `er3t/pre/cld` module calculates extinction, thermodynamic phase, and effective
580 droplet radius of clouds from the input data. The `er3t/pre/pha` module creates the required
581 single scattering albedo and scattering phase function. The default is a Henyey-Greenstein phase
582 function with a fixed asymmetry parameter of 0.85. Along with the current distribution (v0.1.0) of
583 EaR^{3}T, the Mie phase functions based on thermodynamic phase, effective droplet radius, and
584 wavelength are supported. In this study, App. 1 and App. 2 use Mie phase functions calculated
585 from Legendre polynomial coefficients (originally distributed along with libRadtran) based on the
586 wavelength and cloud droplet effective radius. In the future, EaR^{3}T will include stand-alone phase
587 functions, which can be chosen on the basis of droplet size distributions in addition to effective

594   radius. It is also possible to include aerosols in a similar fashion as clouds. This is done with the

595   `er3t/pre/aer` module. In the case of aerosols, spectral single scattering albedo and asymmetry

596   parameter are required as inputs in addition to the extinction fields.

597   After the optical properties are calculated, they are passed into the 3D-RT step

598   (`er3t/rtm/mca`). In addition to MCARaTS, planned solvers for the future include MYSTIC

599   (Monte Carlo code for the physically correct tracing of photons in cloudy atmospheres, Mayer,

600   2009) and SHDOM (Spherical Harmonic Discrete Ordinate Method, Evans, 1998; Pincus and

601   Evans, 2009). This step performs the setup of RT solver-specified input parameters and data files,

602   distributing runs over multiple Central Processing Units (CPUs), and post-processing RT output

603   files into a single, user-friendly HDF5 file. For example, when radiance is specified as output

604   (default in App. 1 and App. 2), key information such as the radiance field and its standard deviation

605   are stored in the final HDF5 file (details see Table 1).

606   While the EaR^{3}T repository comes with various applications such as App. 1 and App. 2,

607   described above, the functions used by these master or 'wrapper' programs can be organized in

608   different ways, where the existing applications serve as templates for a quick start when developing

609   new applications. The functions used by the master code pass information through the various

610   steps as Python objects. For example, in `examples/01_oco2_rad-sim.py`, the downloaded

611   and processed satellite data are stored into the `sat` object. Later, the `sat` object is passed into an

612   EaR^{3}T function to create the `cld` object that contains cloud optical properties. Similarly, EaR^{3}T

613   provides functions to create the `atm`, and `sfc` objects with optical properties for atmospheric

614   gases and the surface. These objects (`atm`, `cld`, `sfc`) are in turn passed on to solver-specific

615   modules for performing RT calculations. The user can choose to save the data of the intermediate

616   objects into Python pickle files after the first run. In this way, multiple calls with identical input

617   can re-use existing data, which accelerates the processing time of EaR^{3}T. Unless the user specifies

618   the `overwrite` keyword argument in the object call to reject saving pickle files, these shortcuts

619   save significant time. Moreover, EaR^{3}T is capable of distributing simulations over multiple CPUs

620   to accelerate the calculations, which is useful for potential future application of later EaR^{3}T or

621   EaR^{3}T-like codes in operational or large-scale data processing.

622   In the following sections, we discuss results obtained from EaR^{3}T, starting with those from

623   `examples/01_oco2_rad-sim.py` and `examples/02_modis_rad-sim.py` (section

624   4), `examples/03_spns_flux-sim.py` (section 5), and concluding with

632 `examples/04_cam_nadir_rad-sim.py` (section 6). The detailed RT setup for the
633 applications is provided Table A1 in Appendix A.

635

4. EaR³T as a 3D Satellite Radiance Simulator

637   This section demonstrates the automated 3D radiance simulation for satellite instruments
638 by EaR³T for OCO-2 and MODIS measured radiance based on publicly available MODIS retrieval
639 products. The OCO-2 application is an example of radiance consistency between two distinct
640 satellite instruments where the measurements of one (here, OCO-2) are compared with the
641 simulations based on data products from the other (here, MODIS). The MODIS application, on
642 the other hand, is an example of radiance self-consistency. We will show how inconsistencies can
643 be used for detecting cloud and surface property retrieval biases.

4.1 OCO-2 (App. 1)

645   The OCO-2 radiance measurements at 768.52 nm for our sample scene in the context of
646 MODIS imagery were shown in Figure 2. For that track segment, Figure 5a shows the simulated
647 radiance along with the measurements as a function of latitude. The radiance was averaged over
648 every 0.01° latitude window from 37° N to 39° N (the standard deviation within the bin indicated
649 by the shaded color). In clear-sky regions (e.g., around 38.2º N), the simulations (red) are
650 systematically higher than the measurements (black), even though the footprint-level OCO-2
651 retrieval was used to scale the MYD09 surface reflectance field as described in section 2.2.2
652 (Figure 4). This is because, unlike the MYD09 algorithm which relies on multiple overpasses and
653 multiple-days for cloud-clearing, the OCO-2 retrieval is done for any clear footprint. Clouds in the
654 vicinity lead to enhanced diffuse illumination that is erroneously attributed to the surface
655 reflectance itself. The EaR³T IPA calculations of the clear-sky pixels (blue) essentially reverse the
656 3D effect and therefore match the observations better. The 3D calculations enhance the reflectance
657 through the very same 3D cloud effects that led to the enhanced surface illumination in the first
658 place. It is possible to correct this effect by down-scaling the surface reflectance according to the
659 ratio between clear-sky 3D and IPA calculations, but this process is currently not automated.

660

Deleted: four

Deleted: in Table 2

Deleted: ¶

... [1]

Deleted: APP
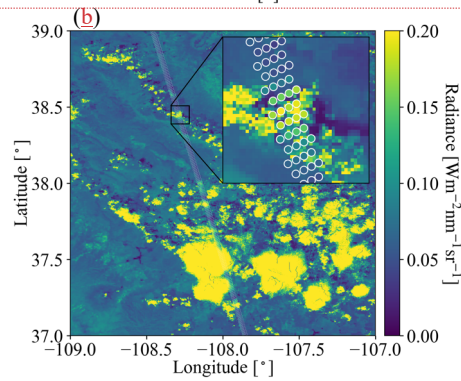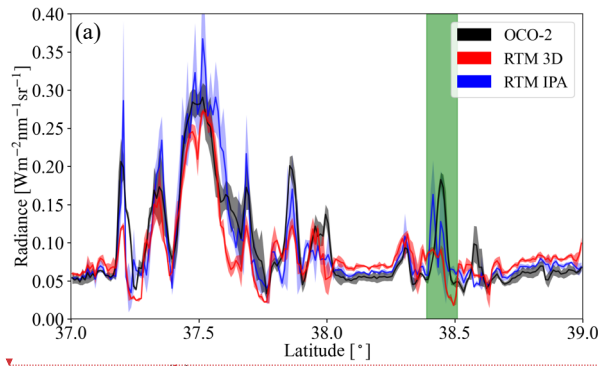
Figure 5. **(a)** Latitudinally averaged (0.01° spacing) radiance calculations from EaR³T (red: 3D, blue: IPA) and OCO-2 measured radiance at 768.52 nm (black) The green shaded area indicates the inset shown in (b). **(b)** The same as Figure 2 except OCO-2 measured radiance overlaid on IPA radiance simulations at 768.52 nm. The solar zenith angle (SZA) for the radiance simulation case is 33.57°.

In the cloudy locations, the IPA calculations match the OCO-2 observations on a footprint-by-footprint level (see Figure 5b), demonstrating that wind and parallax corrections were performed successfully. Of course, there is not always a perfect agreement because of morphological changes in the cloud field over the course of six minutes. It is, however, apparent that the 3D calculations agree to a much lesser extent with the observations than the IPA calculations. Just like the mismatch for the clear-sky pixels indicates a bias in the input surface reflectance, the bias here means that the input cloud properties (most importantly COT) are inaccurate. For most of the reflectance peaks, the 3D simulations are too low, which means that

682   the input COT is biased low. This is due to 3D cloud effects on the MODIS-based cloud retrieval.
683   Since they are done with IPA, any net horizontal photon transport is not considered, which leads
684   to an apparent surface brightening as noted above, at the expense of the cloud brightness. As a
685   result, the COT from darker clouds is significantly underestimated. This commonly known
686   problem (Barker and Liu, 1995), with several aspects discussed in the subsequent EaR^{3}T
687   applications, can be identified by radiance consistency checks such as the one shown in Figure 5,
688   and mitigated by novel types of cloud retrievals that do take horizontal photon transport into
689   account (section 6).
690

691   **4.2 MODIS (App. 2)**

692   To go beyond the OCO-2 track and understand the bias between simulated and observed
693   radiances from a domain perspective, we now consider the radiance simulations for the MODIS
694   650 nm channel. The setup is exactly the same as for the OCO-2 simulations, except that 1) the
695   viewing zenith angle is set to the average viewing zenith angle of MODIS within the shown domain
696   (instead of OCO-2), and 2) the surface reflectances from MYD09 are used directly, this time from
697   the 650 nm channel without rescaling. Figure 6a shows the MODIS measured radiance field, while
698   Figure 6b shows the EaR^{3}T 3D simulations. Visually, the clouds from the EaR^{3}T simulation are
699   generally darker than the observed clouds, which is in line with our aforementioned explanation
700   of net horizontal photon transport. They are also blurrier because radiative smoothing (Marshak et
701   al., 1995) propagates into the retrieved COT fields, which are subsequently used as input to EaR^{3}T.
702   To look at darkening and smoothing effects more quantitatively, Figure 7 shows a heatmap plot of
703   simulated radiance versus observed radiance. It shows that the radiance for cloud-covered pixels
704   (labeled "cloudy") from EaR^{3}T are mostly low-biased while good agreement between simulations
705   and observations was achieved for clear-sky radiance (labeled "clear-sky"). The good agreement
706   over clear-sky regions is expected. As mentioned above, we use MYD09 as surface reflectance
707   input, which in contrast to the OCO-2 surface reflectance product is appropriately cloud-screened
708   and therefore does not have a reflectance high bias. There is, of course, a reflectance enhancement
709   in the vicinity of clouds, but that is captured by the EaR^{3}T calculations. The fact that the
710   calculations agree with the observations even for clear-sky pixels in the vicinity of clouds, shows
711   that the concept of radiance consistency works to ensure correct satellite retrievals even in the
712   presence of clouds. It also corroborates our observation from section 4.1 that COT$_{IPA}$ is low biased.

714   Since the MODIS reflectance is *not* self-consistent with respect to COT$_{IPA}$ as shown for the *cloudy*

715   pixels in Figure 7, we can identify a bias in the cloud properties even without knowing the ground

716   truth of COT. On the other hand, successful closure in radiance (self-consistency) would provide

717   an indication that the input fields including COT are accurate, although it is certainly a weaker

718   metric than direct verification of the retrievals through aircraft satellite retrieval validation with

719   in-situ instruments.

720
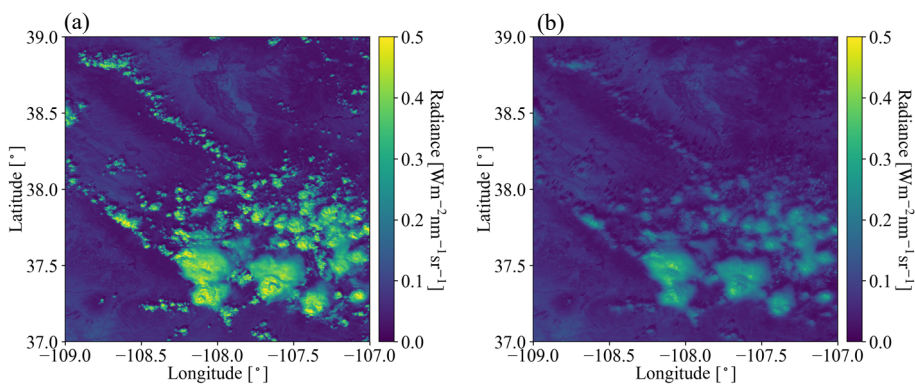
721

722   **Figure 6**. **(a)** MODIS measured radiance in channel 1 (650 nm). **(b)** Simulated 3D radiance at 650 nm from EaR^{3}T.

723   The solar zenith angle for the radiance simulation case is 34.42°.

724
725
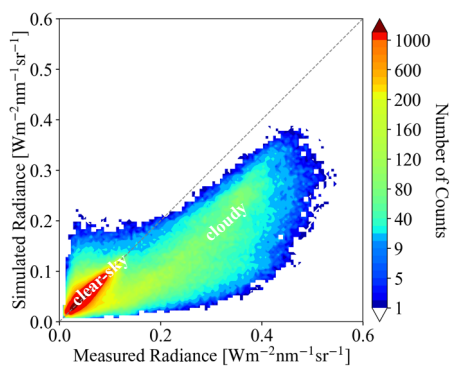
726

727   **Figure 7**. Heatmap plot of EaR^{3}T simulated 3D radiance vs. MODIS measured radiance at 650 nm.

728

729   Summarizing the two satellite radiance simulator applications, one can say that EaR³T

730 enables a radiance consistency check for inhomogeneous cloud scenes. We demonstrated that a

731 lack of simulation-observation consistency (MODIS versus OCO-2) and self-consistency (MODIS

732 versus MODIS) can be traced back to biased surface reflectance or cloud fields in the simulator

733 input. This can become a diagnostic tool for the quality of retrieval products from future or current

734 missions, even when the ground truth is not known. It should be pointed out that the vertical extent

735 of the clouds affects the simulated radiance – the larger the vertical extent, the larger the 3D effects

736 (more horizontal photon transport). Since we make the assumption of a cloud geometric thickness

737 of 1 km if no thickness information is provided, the simulated radiance at the satellite sensor level

738 is valid for that proxy cloud only. For deeper clouds, the simulated radiance would be even lower.

739 Either way, the comparison with the actual radiance measurements will reveal a lack of closure.

740 Additionally, although the clouds introduce the lion's share of the 3D bias that is identified by the

741 radiance consistency check, additional discrepancies can be introduced in different ways. For

742 example, the topography (mountainous region in Colorado) is not considered by MCARaTS (it is

743 considered by MYSTIC, but this solver has not been implemented yet).

744   For technical reference: The MODIS simulation (domain size of [Nx=1188, Ny=1188])

745 took about one hour on a Linux workstation with 12 CPUs for three 3D RT runs with 10^8 photons

746 each. With a slightly modified setup and parallelization, the automation can be easily applied for

747 entire satellite orbits, although more research is required to optimize the computation speed

748 depending on the desired output accuracy.

749

750 **5. EaR³T as 3D Aircraft Irradiance Simulator (App. 3)**

751   In contrast to the previous applications that focused on satellite remote sensing, we will

752 now be applying EaR³T to quantify 3D cloud retrieval biases through direct, systematic validation

753 of imagery-derived *irradiances* against aircraft measurements, instead of using the indirect path

754 of radiance consistency in section 4. Previous studies (e.g., Schmidt et al., 2007; Kindel et al.,

755 2010) conducted radiative closure between remote sensing derived and measured irradiance using

756 isolated flight legs as case studies. Here, with the efficiency afforded by the automated nature of

757 EaR³T, we are able to conduct radiative closure of irradiance through a statistical approach that

758 employs campaign-scale amounts of measurement data. Specifically, we used EaR³T to perform

759 large-scale downwelling irradiance simulations at 745 nm based on geostationary cloud retrievals

Deleted: APP

761 from AHI for the CAMP^{2}Ex campaign, and directly compare these simulations to the SPN-S
762 measured irradiances onboard the P-3 aircraft. This is done for all below-cloud legs from the entire
763 campaign with the aim to assess the degree to which satellite-derived near-surface irradiances
764 reproduce the true conditions below clouds.

765   The irradiance simulation process is similar to the previously described radiance simulation
766 in section 4, with only a few modifications. First, we used cloud optical properties from the AHI
767 cloud product (COT, CER and CTH) as direct inputs into EaR^{3}T. Secondly, we used a constant
768 ocean surface reflectance value of 0.03. Such simplification in surface albedo is made under the
769 assumption that 1) the ocean surface is calm with no whitecaps, and that 2) the Lambertian
770 bidirectional reflectance distribution function (BRDF) is sufficient (instead of directionally
771 dependent BRDF) to represent surface albedo for the irradiance calculation. Since the ocean
772 surface albedo can greatly differ from 0.03 when the Sun is extremely low (Li et al., 2006), we
773 excluded data under low-Sun conditions where the SZA is greater than 45°. Lastly, since EaR^{3}T
774 can only perform 3D simulations for a domain at a single specified solar geometry, we divided
775 each CAMP^{2}Ex research flight into small flight track segments where each segment contains 6
776 minutes of flight time. The size and shape of the flight track segments can vary significantly due
777 to the aircraft maneuvers, aircraft direction, aircraft speed, etc. For each flight track segment,
778 EaR^{3}T performs irradiance simulations for a domain that extends half a degree at an averaged solar
779 zenith angle. In contrast to the radiance simulation output, which is two-dimensional at a specified
780 altitude and sensor geometry, the irradiance simulation output is three dimensional. In addition to
781 x (longitude) and y (latitude) vectors, it has a vertical dimension along z (altitude). From the
782 simulated three-dimensional irradiance field, the irradiance for the flight track segment is linearly
783 interpolated to the x-y-z location (longitude, latitude, and altitude) of the aircraft. EaR^{3}T
784 automatically sub-divides the flight track into tiles encompassing track segments, and extracts the
785 necessary information from the aircraft navigational data. Based on the aircraft time and position,
786 EaR^{3}T downloads the AHI cloud product that is closest in time and space to the domain containing
787 the flight track segment.

788   Figure 8 shows the simulated irradiance for a sample flight track below clouds on 20
789 September, 2019. Figure 8a shows the flight track overlaid on AHI imagery. Figure 8b shows 3D
790 (in red) and IPA (in blue) downwelling irradiance simulations for the highlighted flight track in
791 Figure 8a, as well as measurements by the SPN-S (in black). Since the 3D and IPA simulations

are performed separately at discrete solar and sensor geometries for each flight track segment based on potentially changing cloud fields from one geostationary satellite image to the next, discontinuities in the calculations (indicated by gray dashed lines) are expected. The diffuse irradiance (downwelling and upwelling) can also be simulated and compared with radiometer measurements (not shown here). Since the irradiance was simulated/measured below clouds, high values of downwelling irradiance indicate thin-cloud or cloud-free regions while low values of downwelling irradiance indicate thick-cloud regions. The simulations successfully captured this general behavior – clouds thickened from west to east until around 121.25° E, and thinned eastwards. However, the fine-scale variabilities in irradiance were not captured by the simulations due to the coarse resolution of COT in the AHI cloud product (3-5 km). Additionally, the simulations also missed the clear-sky regions in the very east and west of the flight track as indicated by high downwelling irradiance values measured by SPN-S. This is probably also due to the coarse resolution of the AHI COT product where small cloud gaps are not represented. Large discrepancies between simulations and observations occur in the mid-section of the flight track where clouds are present (e.g., longitude range from 121.15° to 121.3°). Although the 3D calculations differ somewhat from the IPA results, they are both biased high, likely because the input COT (the IPA-retrieved AHI product) is biased low. This bias is caused by the same mechanism that was discussed earlier in the MODIS examples (section 4.2). This begs the question whether this is true for the entire field mission. To answer the question, we performed a *systematic* comparison of the cloud transmittance for *all* available below-cloud flight tracks from CAMP^{2}Ex, using EaR^{3}T's automated processing pipeline. The output of this pipeline is visualized in time-synchronized flight videos (Chen et al., 2022), which show the simulations and observations along all flight legs point by point. These videos give a glimpse of the general cloud environment during the field campaign from the geostationary satellite perspective.

824

825
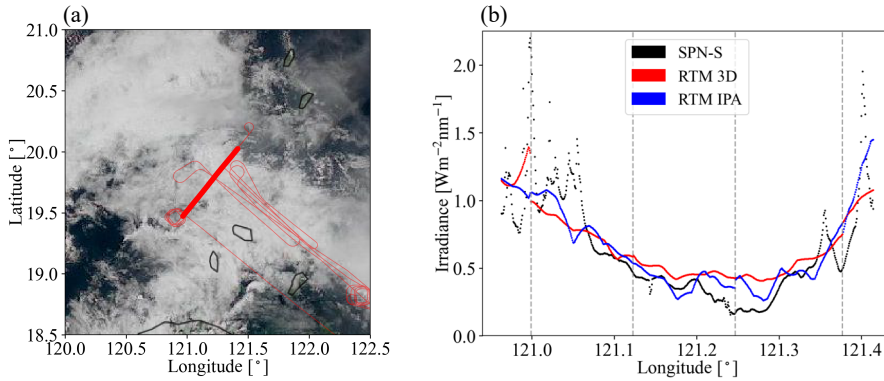
Figure 8. **(a)** Flight track overlay HIMAWARI AHI RGB imagery over the Philippine Sea on 20 September, 2019. The thin line shows the entire flight track within the domain. The thick line highlights the specific leg analyzed in (b). **(b)** Measured downwelling irradiance from SPN-S at 745 nm and calculated 3D and IPA irradiance from EaR³T for the highlighted flight track in (a).

For this comparison, we use transmittance instead of irradiance. The transmittance is calculated by dividing the downwelling irradiance below clouds ($F_\downarrow^{bottom}$) by the downwelling irradiance at the top of the atmosphere extracted from the Kurucz solar spectra ($F_\downarrow^{TOA}$; Kurucz, 1992) at incident solar zenith angle (SZA), where $Transmittance = F_\downarrow^{bottom} \big/ (F_\downarrow^{TOA} \cdot \cos(SZA))$. Thus the transmittance has less diurnal dependence than the irradiance. Figure 9 shows the histograms of the simulated and measured cloud transmittance from all below-cloud legs. The average values are indicated by dashed lines. Although the averaged values of IPA and 3D transmittance are close, their distributions are different. Only the 3D calculations and the measured transmittance reach values beyond 1. This occurs in clear-sky regions in the vicinity of clouds that receive photons scattered by the clouds as previously discussed for the OCO-2 application.

Deleted: because it has less diurnal dependence

Deleted: completely
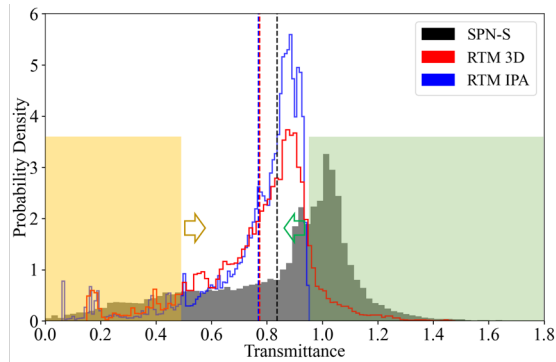
845

846 **Figure 9**. Histogram of measured transmittance from SPN-S at 745 nm (black) and calculated 3D (red) and IPA (blue)

847 transmittance from EaR³T for all the below-cloud flight tracks during CAMP²Ex in 2019. The mean values

848 are indicated by dashed lines. The yellow (green) shaded area represents the relatively low (high)

849 transmittance region where the probability density of the observed transmittance (black) is greater than the

850 calculations.

851

852 Both the distribution and the mean value of the simulations are different from the

853 observations – the simulation histograms peak at around 0.9 while the observation histogram peaks

854 at around 1. The histograms indicate that the RT simulations miss most of the clear-sky conditions

855 because of the coarse resolution of the AHI cloud product. If clouds underfill a pixel, AHI

856 interprets the pixel as cloudy in most cases. This leads to an underestimation of clear-sky regions

857 since cumulus and high cirrus were ubiquitous during CAMP²Ex. The area on the left (highlighted

858 in yellow) has low cloud transmittance associated with thick clouds. In this range, the histograms

859 of the calculations are generally below the observations, and the PDF of the calculations is offset

860 to the right (indicated by the yellow arrow). This means that the transmittance is overestimated by

861 both IPA and 3D RT, and thus that the COT of thick clouds is underestimated, consistent with

862 what we found before (Figure 8b). The high-transmittance end (highlighted in green) is associated

863 with clear-sky and thin clouds. Here, the peak of the PDF is shifted to the left (green arrow), and

864 the calculations are biased low. This is caused by a combination of 1) the overestimation in COT

865 of thin clouds due a 3D bias in the AHI IPA retrieval, 2) the aforementioned resolution effect that

866 underestimates the occurrence of clear-sky regions (or overestimation in cloud fraction), and 3)

867 net horizontal photon transport from clouds into clear-sky pixels. Overall, the calculations

868 underestimate the true transmittance by 10%. This might seem to contradict Figure 7, where the

876 calculated reflected radiance was biased low due to the *underestimation* of COT in the heritage
877 retrievals, which would correspond to an *overestimation* of the radiation transmitted by clouds.
878 This effect is indeed apparent in the yellow-shaded area of Figure 9 (high COTs), but the means
879 (dashed lines) show exactly the opposite. To understand that, one has to consider that the histogram
880 depicts all-sky conditions, which include both cloudy and clear pixels. In this case, the direction
881 of the overall (all-sky) bias follows the direction of the thin-cloud/clear bias, rather than the
882 direction of the thick cloud bias. For different study regions of the globe with different cloud
883 fractions, cloud size distributions, and possibly different imager resolutions, the direction and
884 magnitude of the bias might be very different.

885   Summarizing, this application demonstrates that the EaR^{3}T's automation feature allows
886 systematic simulation-to-observation comparisons. If aircraft observations are available, then
887 closure between satellite-derived irradiance and suborbital measurements is a more powerful
888 verification of satellite cloud retrieval products than the radiance consistency from the earlier
889 stand-alone satellite applications. Even more powerful is the new approach to process the data
890 from an entire field mission for assessing the quality of cloud products in a region of interest (in
891 this case, the CAMP^{2}Ex area of operation).

892

893 **6. EaR^{3}T for Mitigating 3D Cloud Retrieval Biases (App. 4)**

894   In this section, we will use high-resolution imagery from a radiometrically calibrated
895 all-sky camera flown during the CAMP^{2}Ex to isolate the 3D bias (sometimes referred to as IPA
896 bias) and explore its mitigation with a newly developed CNN cloud retrieval framework (Nataraja
897 et al., 2022). The CNN, unlike IPA, takes pixel-to-pixel net horizontal photon transport into
898 account. It exploits the spatial context of pixels in cloud radiance imagery, and extracts a higher-
899 dimensional, multi-scale representation of the radiance to retrieve COT fields as the output. It does
900 so by learning on "training data", which in this case was input radiance and COT pairs synthetically
901 generated by EaR^{3}T using LES data from the Sulu Sea. The best CNN model, trained on different
902 coarsened resolutions of the data pairs, is included within the EaR^{3}T repository. For App. 4, this
903 CNN is applied to real imagery data for the first time, which in our case are near-nadir observations
904 by the all-sky camera (section 2.2.5) that flew in CAMP^{2}Ex.

905   The CNN model was trained at a single (fixed) sun-sensor geometry (solar zenith angle,
906 SZA=29.2°; solar azimuth angle, SAA=323.8°, viewing zenith angle, VZA=0º), at a spatial

Deleted: We found that the bias between observed and satellite-derived cloud transmittance is partially caused by the coarse imager resolution, and partially by 3D effects, although other retrieval artifacts could also play a role. Although important for future research, it is beyond the scope of this paper to disentangle these effects.

Deleted: APP

Deleted: a

Deleted: -

Deleted: APP

Formatted: Indent: First line: 0.5"

917 resolution of 100 m. We therefore chose a camera scene with a matching SZA (28.9°), and rotated

918 the radiance imagery to match SAA=323.8°, and subsequently gridded the 8-12 m native

919 resolution camera data to 100 m. Figure 10a shows the RGB imagery captured by the all-sky

920 camera over the Philippine Sea at 02:10:06 UTC on 5 October 2019. The Sun is located at the

921 southeast (as indicated by the yellow arrow) and can be easily identified from the sun glint. Note

922 that this image has not yet been geolocated; it is depicted as acquired in the aircraft reference frame.

923 Figure 10b shows the rotated scene of the red channel radiance for the region encircled in yellow

924 in Figure 10a. The sun (as indicated by the yellow arrow) is now at SAA=323.8°. The selected

925 study region is indicated by the red rectangle in Figure 10b (6.4x6.4 km^2), where the raw radiance

926 of the camera is gridded at 100 m resolution to match the spatial resolution of the training dataset

927 of the CNN.

Deleted: core area	

Deleted: gridded radiance field is shown instead of the native-resolution imagery	

928

929 (a)
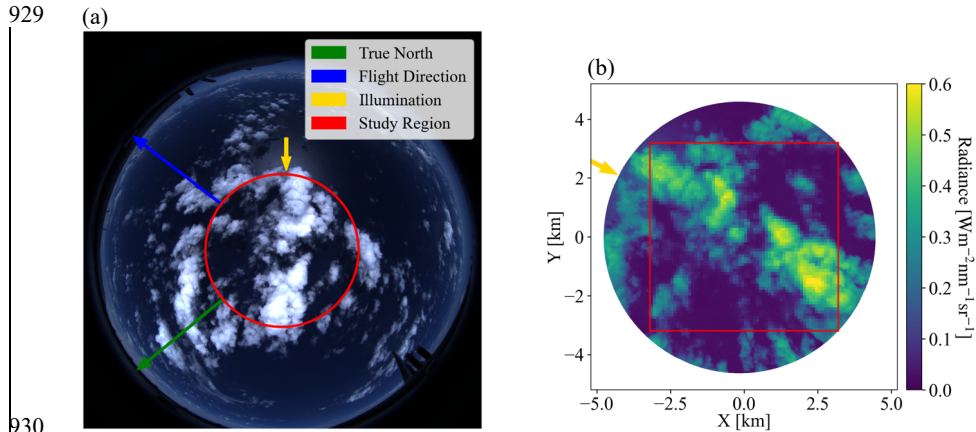
930

931 **Figure 10**. **(a)** RGB imagery of nadir-viewing all-sky camera deployed during CAMP^{2}Ex for a cloud scene centered

932 at [123.392°E, 15.2744°N] over the Philippine Sea at 02:10:06 UTC on 5 October, 2019. The arrows

933 indicate the true north (green), flight direction (blue), and illumination (where the sunlight comes from,

934 yellow). **(b)** Red channel radiance measured by the camera for the circular area indicated by the red circle

935 in (a). Red squared region shows gridded radiance with a pixel size of 64x64 and spatial resolution of 100

936 m.

Deleted: lines	
Deleted: axis of the aircraft	
Deleted: yellow	
Deleted: and wing to wing	
Deleted: across, black	
Deleted: The yellow circle shows the approximate field of view that is geolocated for (b); the dots denote various directions from the nadir point. **(b)** Gridded radiance for the square area indicated by solid black lines in (a) with a pixel size of 64x64 and spatial resolution of 100 m	

937

938 From the radiance field, we used both the traditional IPA (based on the two-stream

939 approximation) and the new CNN to retrieve COT fields. Figure 11 shows the COT$_{IPA}$ and COT$_{CNN}$

Deleted: Later for the comparison of COT and RT calculations, only the data from the red square box (50x50) is used. The solar position (azimuth) is indicated by the yellow arrow.	

957 fields, which are visually quite different. For relatively thin clouds (e.g., at around {2, 1.8}), the

958 CNN tends to retrieve larger COT values than COT_{IPA}. Also, it returns more spatial structure than

959 the IPA (e.g., around {2,-1}). To assess how either retrieval performs, we now apply the radiance

960 self-consistency approach introduced with MODIS data in section 4.2. Using both the IPA and the

961 CNN retrieval as input, we had EaR^3T calculate the (synthetic) radiance that the camera should

962 have observed if the retrieval were accurate. The clouds are assumed to be located at 1-2 km. Such

963 an assumption is inferred from low-level aircraft observations of clouds on the same day. These

964 radiance fields are shown in Figure 12a and 12b, and can be compared to Figure 12c. Seven edge

965 pixels have been removed from the original domain because the CNN performs poorly at edge

966 pixels, and because the 3D calculations use periodic boundary conditions.
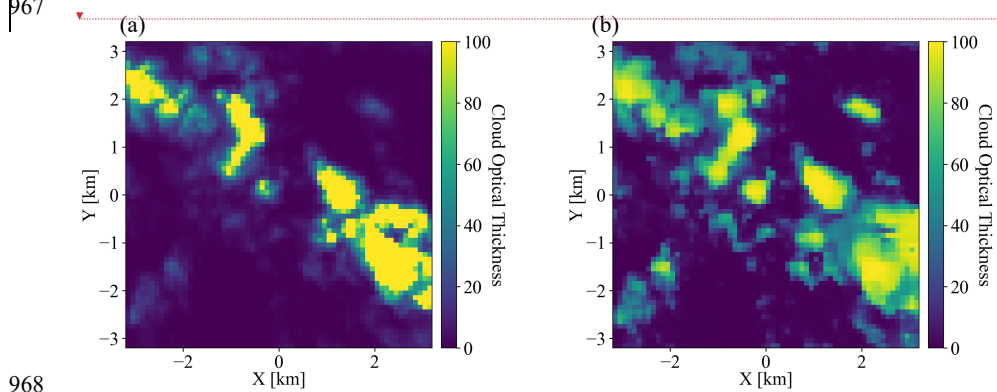
967

968
969 **Figure 11**. Cloud optical thickness for the gridded radiance in Figure 10b **(a)** estimated by IPA and **(b)** predicted by
970   CNN.

989

990

991
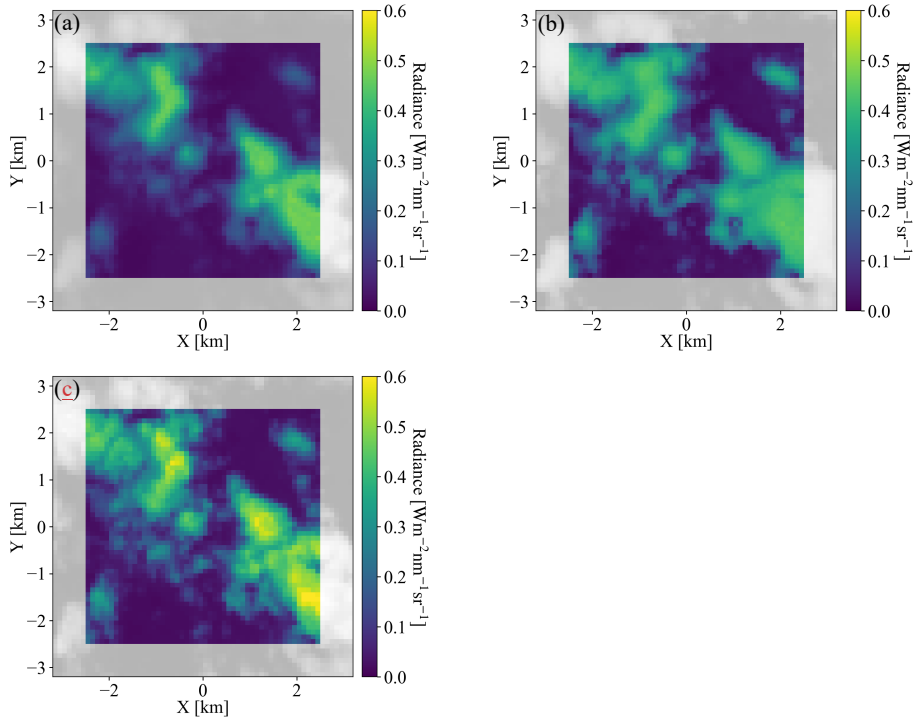
Figure 12. 3D radiance calculations from EaR³T at 600 nm based on cloud optical thickness field **(a)** estimated by

JPA, and **(b)** predicted by the CNN. The radiance measured by the all-sky camera (the same as Figure 10b) is provided in the same format at **(c)** for comparison. The calculations were originally performed for the 64x64 domain. Then 7 pixels along each side of the domain (contoured in gray) were excluded, which resulted in a 50x50 domain.

| Deleted: Two-Stream approximation |
| Deleted: and |
| Formatted: Font: Bold |

| Deleted: ¶ |
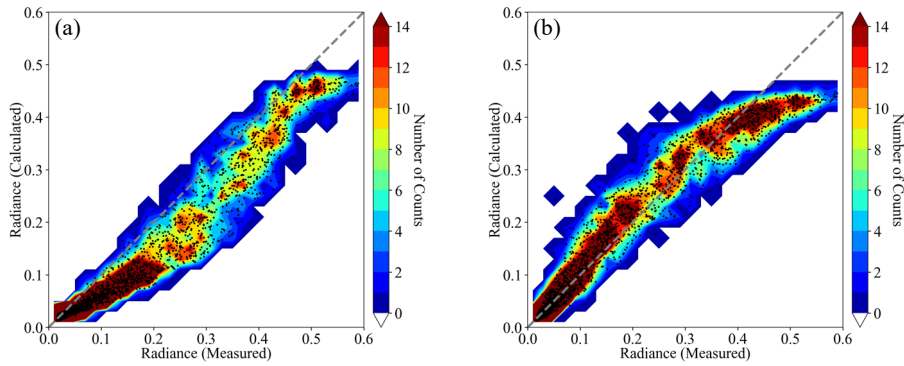
Figure 13. Scatter plot overlays 2D histogram of 3D radiance calculations at 600 nm based on cloud optical thickness **(a)** estimated by IPA and **(b)** predicted by the CNN vs. measured red channel radiance from all-sky camera.

As evident from the brightest pixels in Figures 12b and 12c, the radiances simulated on the basis of the CNN COT input are markedly lower than actually observed by the camera. This is because the CNN was trained on a LES dataset with limited COT range that excluded the largest COT that occurred in practice. This means that the observational data went beyond the original training envelope of the CNN, which highlights the importance of choosing the CNN training data carefully for a given region. In Figure 13, the simulations are directly compared with the original observations, confirming that indeed the CNN-generated data are below the observations on the high radiance end. Otherwise, the CNN-generated radiances agree with the observations. In contrast, the IPA-generated data are systematically lower than the observations, over the dynamic range of the COT, which is indicative of the 3D retrieval bias that we discussed earlier. Here again, the self-consistency approach proves useful despite the absence of ground truth data for the COT. This is extremely helpful because in reality satellite remote sensing does not have the ground truth of COT, whereas radiance measurements are always available. For the CNN, the self-consistency of the radiance is remarkable for the thinner clouds (radiance smaller than 0.4), which encompass 83.5% of the total number of image pixels.

Finally, we use EaR^{3}T to propagate the 3D cloud retrieval bias into the associated bias in estimating the cloud radiative effect from passive imagery retrievals, which means that we are returning from a remote sensing to an energy perspective (irradiance) at the end of the paper. The calculated cloud radiative effects (CRE) of both below-clouds (at the surface) and above-clouds

1028 (at 3 km) are shown in Figure 14a and 14b. The most important histograms are those from 3D

1029 irradiance calculations based on the CNN retrievals (gray solid line), as this combination would

1030 be used in a next-generation framework for deriving CRE from passive remote sensing, and the

1031 other would be IPA irradiance calculations based on the IPA retrieval (red solid line), as done in

1032 the traditional (heritage) approach. The dashed lines are the other combinations. The mean values

1033 (red vs. gray) indicate that in our case the traditional approach would lead to a high bias of more

1034 than to 25% both at the surface and above clouds. Here again, 3D biases do not cancel each other

1035 out in the domain average. If the CNN had better fidelity even for optically thick clouds, the real

1036 bias in CRE would be even larger. A minor, but interesting finding is that regardless of which COT

1037 retrieval is used, the mean CRE is very similar for IPA and 3D irradiance calculations (e.g.,

1038 $\overline{CRE_{IPA}(COT_{CNN})} \approx \overline{CRE_{3D}(COT_{CNN})}$, blue dashed line overlay gray solid line), even though the

1039 PDFs are very dissimilar. By far the largest impact on accuracy comes from the retrieval technique,

1040 not from the subsequent CRE calculations. Here again, the self-consistency check turns out as a

1041 powerful metric to assess retrieval accuracy. Of course, we only used a single case in this part of

1042 the paper. For future evaluation of the CNN versus the IPA, one would need to process larger

1043 quantities of data in an automated fashion as done in the first part of the paper. This is beyond the

1044 scope of this introductory paper, and will be included in future releases of EaR^{3}T and the CNN.

1045
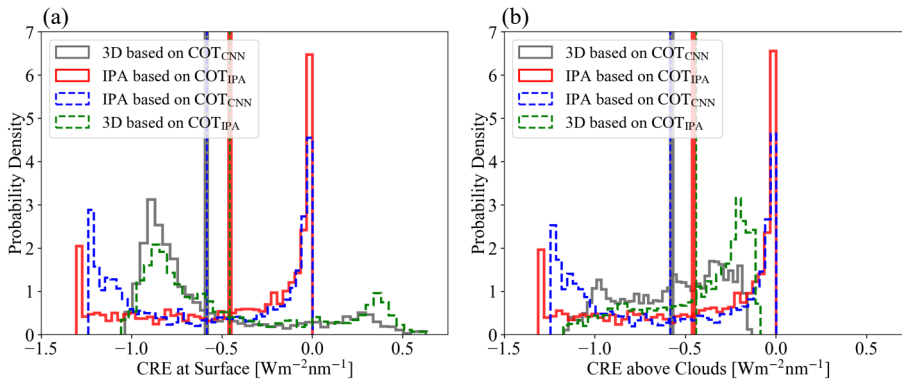
1046
1047 **Figure 14**. Histograms of cloud radiative effects derived from 1) 3D irradiance calculations based on COT$_{CNN}$ (solid

1048 gray), 2) IPA irradiance calculations based on COT$_{IPA}$ (solid red), 3) IPA irradiance calculations based on

1049 COT$_{CNN}$ (dashed blue), and 4) 3D irradiance calculations based on COT$_{IPA}$ (dashed green) both **(a)** at the

1050 surface and **(b)** above the clouds. The mean values are indicated by vertical lines.

1051

7. Summary and Conclusion

In this paper, we introduced EaR^{3}T, a toolbox that provides high-level interfaces to automate and facilitate 1D- and 3D-RT calculations. We presented applications that used EaR^{3}T to:

a) build a processing pipeline that can automatically simulate 3D radiance fields for satellite instruments (currently OCO-2 and MODIS) from publicly available satellite surface and cloud products at any given time over any specific region;

b) build a processing pipeline that can automatically simulate irradiance along all flight legs of aircraft missions, based on geostationary cloud products;

c) simulate radiance and irradiance for high-resolution COT fields retrieved from an airborne camera, using both a traditional 1D-RT (IPA) approach, and a newly developed 3D-RT (CNN) approach that considers the spatial context of a pixel.

Unlike other satellite simulators that employ 1D-RT, EaR^{3}T is capable of performing the radiance and irradiance calculations in 3D-RT mode. Optionally, it can be turned off to link back to traditional 1D-RT codes, and to calculate 3D perturbations by considering the changes of 3D-RT fields relative to the 1D-RT baseline.

With the processing pipeline under a) (App. 1 and App. 2, section 4), we prototyped a 3D-RT powered radiance loop that is envisioned for upcoming satellite missions such as EarthCARE and AOS. Retrieved cloud fields (in our case, from MODIS and from an airborne camera) are fed back into a 3D-RT simulation engine to calculate at-sensor radiances, which are then compared with the original measurements. Beyond currently included sensors, others can be added easily, taking advantage of the modular design of EaR^{3}T. This radiance closure loop facilitates the evaluation of passive imagery products, especially under spatially inhomogeneous cloud conditions. The automation of EaR^{3}T permits calculations at any time and over any given region, and statistics can be built by looping over entire orbits as necessary. The concept of radiance consistency could be valuable even for existing imagery datasets because it allows the automated quantification of 3D-RT biases even without ground truth such as airborne irradiance from suborbital activities. In the future it should be possible to include a 3D-RT pipeline such as EaR^{3}T into operational processing of satellite derived data products.

Benefitting from the automation of EaR^{3}T in b) (App. 3, section 5), we performed 3D-RT irradiance calculations for the entire CAMP^{2}Ex field campaign, moving well beyond radiation

Deleted: APP

Deleted: APP

Deleted: -

Deleted: APP

closure case studies, and instead systematically evaluating satellite-derived radiation fields with aircraft data for an entire region. From the comparison based on all below-cloud flight tracks during the entire campaign, we found that the satellite-derived cloud transmittance was biased low by 10% compared to the observations when relying on the heritage satellite cloud product.

From the statistical results of the CAMP²Ex irradiance closure in b), we concluded that the bias between satellite-derived irradiances and the ground truth from aircraft measurements was due to a combination of the coarse spatial resolution of the geostationary imagery products, and 3D-RT effects. To minimize the coarse-resolution part of the bias and thus to isolate the 3D-RT bias, we used high-resolution airborne camera imagery in c) (App. 4, section 6), and found that even with increased imager resolution, biases persisted. The at-sensor radiance derived from IPA COT retrievals was inconsistent with the original measurements. For cloudy pixels, the calculated radiance was well below the observations, confirming an overall low bias in IPA COT. This low bias could be largely mitigated with the context-aware CNN developed separately in Nataraja et al. (2022) and included in EaR³T. Of course, this novel technique has limitations. For example, the camera reflectance data went beyond the CNN training envelope, which would need to be extended to larger COT in the future. In addition, the CNN only reproduces two-dimensional clouds fields and does not provide access to the vertical dimension, which will be the next frontier to tackle. Still, the greatly improved radiance consistency from COT_{IPA} to COT_{CNN} indicates that the EaR³T-LES-CNN approach shows great promise for the mitigation of 3D-RT biases associated with heritage cloud retrievals. We also discovered that for this particular case, the CRE calculated from traditional 1D cloud products can introduce a warm bias of at least 25% at the surface and above clouds.

EaR³T has proven to be capable of facilitating 3D-RT calculations for both remote sensing and radiative energy studies. Beyond the applications described in this paper, EaR³T has already been extensively used by a series of on-going research projects such as producing massive 3D-RT calculations as training data for a new generation of CNN models (Nataraja et al., 2022), evaluating 3D cloud radiative effects associated with aerosols (Gristey et al., 2022), creating flight track and satellite track simulations for mission planning etc. More importantly, the strategies provided in this paper put novel machine learning algorithms on a physical footing, opening the door for the mitigation of complexity-induced biases in the near-future. More development effort will be invested into EaR³T in the future, with the goals of minimizing the barriers to using 3D-RT

Deleted: either
Deleted: , or caused by
Deleted:
Deleted: APP
Deleted: warming

1126 calculations, and to promote 3D cloud studies. EaR^{3}T will continue to be an educational tool driven
1127 by graduate students. In the future, we plan to add support for additional publicly available 3D RT
1128 solvers, e.g., SHDOM, as well as built-in support for HITRAN and associated correlated-k
1129 methods. From a research perspective, we anticipate that EaR^{3}T will enable the systematic
1130 quantification and mitigation of 3D-RT biases of imagery-derived cloud-aerosol radiative effects,
1131 and may be the starting point for operational use of 3D-RT for future satellite missions.
1132

Appendix A - Technical Input Parameters of EaR^{3}T

EaR^{3}T provides various functions that can be combined to tailored pipelines for automatic 3D radiative transfer (3D-RT) calculations as described App. 1 – 5 of this paper (App. 1 – 5), as well as for complex research projects beyond. Since EaR^{3}T is written in Python, the modules and functions can be integrated into existing functions developed by the users themselves. Parallelization is enabled in EaR^{3}T by default through multi-processing to accelerate computations. If multiple CPUs are available, EaR^{3}T will distribute jobs for the 3D RT calculations. By default, the maximum number of CPUs will be used. Since EaR^{3}T is designed to make the process of setting up and running 3D-RT calculations simple, some parameters that are unavailable from the input data but are required by the RT solvers are populated via default values and assumptions. However, this does not mean that by using EaR^{3}T, one must use these assumptions; they can be easily superseded by user-provided settings. To facilitate this process, Table A1 provides a detailed list of parameters (subject to change in future updates) that can be controlled and modified by the user. In `examples/02_modis_rad-sim.py`, we defined these user-controllable parameters as global variables for providing easy access to user. In the future, most of the parameters will be controllable through a dedicated configuration file for optimal transparency. These parameters can be changed within the code. For instance, by changing the parameters of `_date` (Line 67 in `examples/02_modis_rad-sim.py`) and `region` (Line 68 in `examples/02_modis_rad-sim.py`) into the following:

```
_date   = datetime.datetime(2022, 2, 10)
_region = [-6.8, -2.8, 17.0, 21.0]
```

one can perform similar RT calculations (as demonstrated in App. 2) for another date and region of interest (here, west Sahara Desert on 10 February, 2022). Note that the cloud detection algorithms we included in the code are imperfect (they only work satisfactorily for the App. 2 case we presented in this paper); for other regions on the globe, they may need to be adjusted. Automation of this feature is planned for the future. In addition, intuitive and simple examples are provided in `examples/00_er3t_mca.py` and `examples/00_er3t_lrt.py` for users who are interested in learning the basics of setting up EaR^{3}T for calculations. At the current stage, only limited documentation is provided. However, community support is available from the author of this paper through Discord[6]. In the near-future, more effort will be invested into documentation

---

[6] https://discord.gg/ntqsguwaWv

1165 to give the user more autonomy in creating new applications that cannot be derived from those

1166 provided in our paper.

1167

Parameters	App. 1 examples/01_oco2_rad-sim.py	App. 2 examples/02_modis_rad-sim.py	App. 3 examples/03_spns_flux-sim.py	App. 4 examples/04_cam_nadir_rad-sim.py	App. 5 examples/05_cnn-les_rad-sim.py
Date	September 2, 2019 Specified at Line 667: **date** And Line 626: **date**	September 2, 2019 Specified at Line 67: **date** And Line 500: **date**	September 20, 2019 Specified at Line 442: **date** And Line 241: **date**	October 5, 2019 Specified at Line 390: **date** And Line 233: **date**	August 29, 2016 Specified at Line 222: **date**
Geographical Region	Specified at Line 668: **extent**	Specified at Line 68: **region**	Variable (depends on aircraft location)	N/A	N/A
Z Grid (Number of Grids/Resolution)	40 / 0.5 km Specified at Line 547: **levels**	40 / 0.5 km Specified at Line 422: **levels**	20 / 1 km Specified at Line 184: **levels**	40 / 0.5 km Specified at Line 192: **levels**	20 / 1km Specified at Line 197: **levels**
Wavelength	770 nm Specified at Line 785: **wavelength**	650 nm Specified at Line 70: **wavelength**	745 nm Specified at Line 443: **wavelength**	600 nm Specified at Line 57: **wavelength**	600 nm Specified at Line 62: **wvl0**
Atmospheric Gas Profile	US standard atmosphere Specified at Line 549: **atm0**	US standard atmosphere Specified at Line 424: **atm0**	US standard atmosphere Specified at Line 186: **atm0**	US standard atmosphere Specified at Line 194: **atm0**	US standard atmosphere Specified at Line 200: **atm0**
Atmospheric Gas Absorption	Case specific Specified at Line 557: **abs0**	Default Absorption Database (Coddington et al., 2008) Specified at Line 431: **abs0**	Default Absorption Database (Coddington et al., 2008) Specified at Line 192: **abs0**	Default Absorption Database (Coddington et al., 2008) Specified at Line 201: **abs0**	Default Absorption Database (Coddington et al., 2008) Specified at Line 202: **abs0**
Cloud Top Height	From MODIS L2 cloud product Specified at Line 306: **cth_2d_l2** And Line 592: **cld0**	From MODIS L2 cloud product Specified at Line 280: **cth_2d_l2** And Line 466: **cld0**	From AHI L2 cloud product Specified at Line 211: **cth_2d** And Lines 215: **cld0**	2 km Specified at Line 217: **cth** And Lines 217: **cld0**	From LES Specified at Line 205: **cld0**
Cloud Geometrical Thickness	1 km Specified at Line 592: **cgt**	1 km And Line 466: **cgt**	1 km Specified at Line 215: **cgt**	1 km Specified at Line 217: **cgt**	From LES Specified at Line 205: **cld0**
Cloud Optical Thickness	Two-Stream Approximation for MODIS L1B Reflectance at 250 m resolution Specified at Line 402: **cot_2d_l1b** And Line 592: **cld0**	Two-Stream Approximation for MODIS L1B Reflectance at 250 m resolution Specified at Line 337: **cot_2d_l1b** And Line 466: **cld0**	From AHI L2 cloud product Specified at Line 201: **cot_2d** And Lines 215: **cld0**	Two-Stream Approximation and CNN for camera red channel radiance/reflectance at 100 m resolution Specified at Lines 285 and 324: **cot_ipa** and **cot_wei** And Lines 217: **cld0**	From LES Specified at Line 205: **cld0**
Cloud Effective Radius	From MODIS L2 Cloud Product Specified at Line 313: **cer_2d_l2**	From MODIS L2 Cloud Product Specified at Line 287: **cer_2d_l2**	From AHI L2 cloud product Specified at Line 202: **cer_2d**	12 micron Specified at Lines 285 and 380:	From LES Specified at Line 205: **cld0**

Parameter					
	And Line 592: **cld0**	And Line 466: **cld0**	And Lines 215: **cld0**	**cer_ipa** and **cer_2d** And Lines 217: **cld0**	
Scattering Phase Function	Mie Specified at Line 598: **pha0** And Line 630: **sca**	Mie Specified at Line 472: **pha0** And Line 504: **sca**	Mie Specified at Line 222: **pha0** And Line 240: **sca**	Henyey-Greenstein (g=0.85) Implicitly specified by default at Line 232: **mcarats_ng** Notes: Lines 207, 208, and 237 can be uncommented (meanwhile commenting out Line 209) to turn on Mie	Henyey-Greenstein (g=0.85) Implicitly specified by default at Line 221: **mcarats_ng**
Surface Albedo	From MODIS Surface Reflectance product and scaled by OCO-2 Specified at Line 520: **oco_sfc_alb_2d** And Line 629: **sfc_2d**	From MODIS Surface Reflectance product Specified at Line 395: **mod_sfc_alb_2d** And Line 503: **sfc_2d**	0.03 Implicitly specified by default at Line 237: **mcarats_ng**	0.03 Specified at Line 236: **surface_albedo**	0 Specified at Line 227: **surface_albedo**
Solar Zenith Angle	From OCO-2 geolocation file Specified at Line 615: **sza** And Line 633: **solar_zenith_angle**	From MODIS geolocation file Specified at Line 489: **sza** And Line 507: **solar_zenith_angle**	Variable (depends on aircraft location and date and time)	28.90° Specified at Line 352: **geometry['sza']** And Line 240: **solar_zenith_angle**	29.16° Specified at Line 228: **solar_zenith_angle**
Solar Azimuth Angle	From OCO-2 geolocation file Specified at Line 616: **saa** And Line 634: **solar_azimuth_angle**	From MODIS geolocation file Specified at Line 490: **saa** And Line 508: **solar_azimuth_angle**	Variable (depends on aircraft location and date and time)	296.83° Specified at Line 353: **geometry['saa']** And Line 241: **solar_azimuth_angle**	296.83° Specified at Line 229: **solar_azimuth_angle**
Sensor Altitude	705 km (satellite altitude) Implicitly specified by default at Line 625: **mcarats_ng**	705 km (satellite altitude) Implicitly specified by default at Line 499: **mcarats_ng**	N/A, three-dimensional irradiance outputs at user-defined Z grid	5.48 km (flight altitude) Specified at Line 354: **geometry['alt']** And Line 242: **sensor_altitude**	705 km (satellite altitude) Implicitly specified by default at Line 221: **mcarats_ng**
Sensor Zenith Angle	From OCO-2 geolocation file Specified at Line 617: **vza** And Line 635: **sensor_zenith_angle**	From MODIS geolocation file Specified at Line 491: **vza** And Line 509: **sensor_zenith_angle**	0° (nadir) Implicitly specified by default at Line 237: **mcarats_ng**	0° (nadir) Implicitly specified by default at Line 232: **mcarats_ng**	0° (nadir) Specified at Line 230: **sensor_zenith_angle**
Sensor Azimuth Angle	From OCO-2 geolocation file Specified at Line 618: **vaa**	From MODIS geolocation file Specified at Line 492: **vaa**	0° (insignificant for nadir)	0° (insignificant for nadir)	0° (insignificant for nadir) Specified at Line 231:

	And Line 636: `sensor_azimuth_angle`	And Line 510: `sensor_azimuth_angle`	Implicitly specified by default at Line 237: `mcarats_ng`	Implicitly specified by default at Line 232: `mcarats_ng`	`sensor_azimuth_angle`
Number of Photons	1×10^8 per run Specified at Line 72: `_photon_sim` And Line 640: `photons`	1×10^8 per run Specified at Line 71: `_photon_sim` And Line 514: `photons`	1×10^7 per run Specified at Line 56: `photon_sim` And Line 246: `photons`	1×10^8 per run Specified at Line 56: `_photon_sim` And Line 246: `photons`	1×10^8 per run Specified at Line 66: `_photon_sim` And Line 234: `photons`
Number of Runs	3 Specified at Line 638: `Nrun`	3 Specified at Line 512: `Nrun`	3 Specified at Line 245: `Nrun`	3 Specified at Line 244: `Nrun`	3 Specified at Line 233: `Nrun`
Mode (3D or IPA)	3D and IPA Specified at Line 786: `solver` And Line 641: `solver`	3D Specified at Line 620: `solver` And Line 515: `solver`	3D and IPA Specified at Lines 380 and 381: `solver` And Line 247: `solver`	3D Specified at Lines 391 and 392: `solver` And Line 247: `solver`	3D Specified at Line 210: `solver` And Line 236: `solver`
Parallelization Mode	Python multi-processing Specified at Line 643: `mp_mode`	Python multi-processing Specified at Line 517: `mp_mode`	Python multi-processing Specified at Line 250: `mp_mode`	Python multi-processing Specified at Line 249: `mp_mode`	Python multi-processing Specified at Line 238: `mp_mode`
Number of CPUs	8 Specified at Line 642: `Ncpu`	8 Specified at Line 516: `Ncpu`	16 Specified at Line 314: `Ncpu` And Line 249: `Ncpu`	12 Specified at Line 248: `Ncpu`	24 on clusters Specified at Line 237: `Ncpu`

Table A1: List of parameters used in the five applications. The line numbers used in the table are referring to the code script of each application. If two line numbers are provided, the first one indicates where the parameter is defined and the second one indicates where the parameter is passed into the radiative transfer setup. Users can change either one for customization purposes.

Appendix B – App. 5 Radiance calculations based on the Large Eddy Simulation

The CNN COT retrieval framework was developed by Nataraja et al. (2022). It adapts a U-Net (Ronneberger et al., 2015) architecture and treats the retrieval of COT from radiance as a segmentation problem – probabilities of 36 COT classes (ranging from COT of 0 to 100) are returned as the final COT retrieved for a given cloud radiance field. It accounts for horizontal photon transport, which is neglected in traditional cloud retrieval algorithms; in other words, for the spatial context of cloudy pixels. It was trained on synthetic cloud fields generated by a Large Eddy Simulation (LES) model, which provides the ground truth of COT. Subsequently, EaR³T was used to calculate 3D-RT radiances at 600 nm for LES cloud fields to establish a mapping between

radiance to COT. Only six LES cases were used to represent the variability of the cloud

morphology. Each of these fields are 480x480 pixels across (spatial resolution of 100 m). These

large fields were mapped onto thousands of 64x64 mini tiles with spatial resolution of 100 m as

described in Nataraja et al., 2022. To keep the training data set small, mini tiles selectively sampled

according to their mean COT and standard deviation. This ensured an even representation of the

dynamic range of COT and its variability, which was termed homogenization of the training data

set. Figure A1 shows a collection of samples from the training data as an illustration. All the

aforementioned simulation setup and techniques in data process are included in the App. 5 example

code, which can be applied to the LES data (a different scene from the 6 scenes) distributed along

with EaR^{3}T.
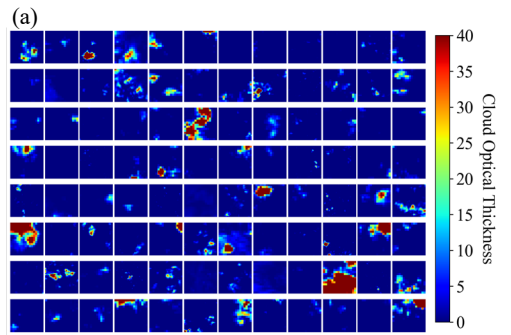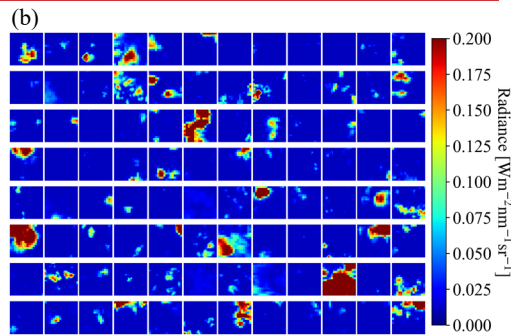
Figure A1. Illustrations of 64x64 tiles of **(a)** cloud optical thickness from LES data and **(b)** calculated 3D radiance from EaR³T for CNN training.

Appendix C

C1. Cloud Detection/Identification

Cloudy pixels are identified through a simple thresholding method based on the red, green, and blue channels of MODIS. When the radiance values of the red, green, and blue channels of a pixel are all greater than the corresponding median value, the pixel is considered as cloudy, as illustrated by the following equation

$$\text{If} \quad \begin{matrix} Red > Median(Red) \ \& \\ Blue > Median(Blue) \ \& \\ Green > Median(Green) \end{matrix} \begin{cases} \textbf{Yes}, \text{cloudy} \\ \textbf{No}, \text{clear sky} \end{cases} \tag{A1}$$

Note that this only works for partially cloud-covered scenes, and may lead to false positives if there is brightness contrast from objects other than clouds. This method was specifically applied for the cases in this paper and should be changed as appropriate for future applications.

C2. Two-Stream Approximation

The two-stream approximation of the reflectance R is calculated using Eq. D2 from Chen et al. (2021), as follows:

$$R = \frac{\tau + \alpha \cdot \left(\frac{2\mu}{(1-g) \cdot (1-\alpha)} \right)}{\tau + \left(\frac{2\mu}{(1-g) \cdot (1-\alpha)} \right)} \tag{A2}$$

where τ is the cloud optical thickness, α is the surface albedo, μ is the cosine of the solar zenith angle, and g is the asymmetry parameter. A value of 0.85 is assumed for g. The domain average of the solar zenith angle and surface albedo are calculated and used for estimating μ and α. Then, for a range of τ, we calculated the R and obtained the relationship of $R(\tau)$. For those cloudy pixels identified through A1, the inverse relationship of $\tau(R)$ is then used for estimating τ at any given R. Note that this approach does not take into account any cloud reflectance anisotropies.

Appendix D

D1. Parallax Correction

1228   From the satellite's view, the clouds (especially high clouds) will be placed at inaccurate

1229 locations on the surface, which have shifted from their actual locations due to the parallax effect.

1230 We followed simply trigonometry to correct for it, as follows:

1231 Longitude correction (positive from west to east):

1232 $$\delta lon = \frac{(z_{cld} - z_{sfc}) \cdot \tan(\theta) \cdot \sin(\phi)}{\pi \cdot R_{Earth}} \times 180° \qquad (B1)$$

1233 Latitude correction (positive from south to north):

1234 $$\delta lat = \frac{(z_{cld} - z_{sfc}) \cdot \tan(\theta) \cdot \cos(\phi)}{\pi \cdot R_{Earth}} \times 180° \qquad (B2)$$

1235 where $(lon_{sat}, lat_{sat}, z_{sat})$ is the satellite location and θ and ϕ (0° at north, positive clockwise)

1236 are the sensor viewing zenith and azimuth angles. z_{cld} and z_{sfc} are the cloud top height and the

1237 surface height. R_{Earth} is the radius of the Earth. Figure A2 shows an illustration of parallax

1238 correction for the cloud field in the inset in Figure 2.

1239

1240 **D2. Wind Correction**

1241   The wind correction aims at correcting the movement of clouds when advected by the wind

1242 between two different satellites' overpasses.

1243 Longitude correction (positive from west to east):

1244 $$\delta lon = \frac{u \cdot \delta t}{\pi \cdot R_{Earth}} \times 180° \qquad (B3)$$

1245 Latitude correction (positive from south to north):

1246 $$\delta lat = \frac{v \cdot \delta t}{\pi \cdot R_{Earth}} \times 180° \qquad (B4)$$

1247 where u and v are the domain-averaged 10 m zonal and meridional wind speeds, and δt is the time

1248 difference between two different satellites that fly on the same orbit. Figure A2 shows the cloud

1249 location after applying the parallax (Appendix D1) and wind correction for the cloud field in the

1250 inset from Figure 2.

1251

1252

1253

Deleted: A1

Deleted: black-boxed cloud field

Deleted: B2

Deleted: A1

Deleted: B1

Deleted: black box
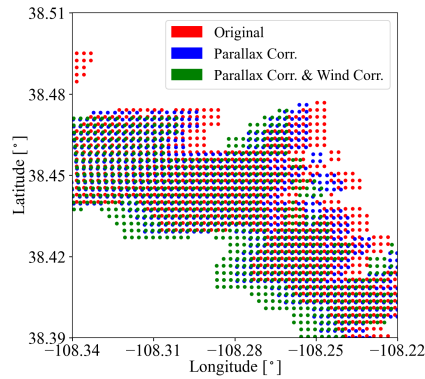
Figure A2. An illustration of correcting cloud location (red) for parallax effect (blue) and wind effect (green) for the cloud field of the inset in Figure 2.

| Deleted: A1 |
| Deleted: black-boxed |

Acknowledgement

The aircraft all-sky camera was radiometrically calibrated by the U.S. Naval Research Laboratory. We thank Jens Redemann for insightful discussions about Figure 9 (App. 3) about the apparent contradiction of the direction of the COT, reflectance, and transmittance biases.

Data availability

For App. 1 and App. 2, the OCO-2 data were provided by the NASA Goddard Earth Sciences Data and Information Services Center (GES DISC, https://oco2.gesdisc.eosdis.nasa.gov/data) and the MODIS data were provided by the NASA Goddard Space Flight Center's Level-1 and Atmosphere Archive and Distribution System (LAADS, https://ladsweb.modaps.eosdis.nasa.gov/archive), which are all publicly available and can be downloaded by EaR³T through the application code. For App. 3, the AHI data were processed by Holz's (coauthor of this paper) team. The SPN-S data were provided by Schmidt and Norgren (coauthors of this paper). Both the AHI and SPN-S data are publicly available at NASA Airborne Science Data for Atmospheric Composition (https://www-air.larc.nasa.gov/missions/camp2ex/index.html). The AHI data and the SPN-S data for the flight track indicated in Figure 8 of the paper are distributed along with EaR³T for demonstration purpose. For App. 4, all sky camera imagery and CNN model are distributed along

with EaR^{3}T. EaR^{3}T is publicly available and can be accessed and downloaded at https://github.com/hong-chen/er3t (or https://doi.org/10.5281/zenodo.7374196 for v0.1.0 used in this paper; Chen and Schmidt, 2022).

Author contributions

All the authors helped with editing the paper. HC developed the EaR^{3}T package in Python including the application code, performed the analysis, and wrote the majority of the paper with input from the other authors. SS provided MCARaTS simulation wrapper code in Interactive Data Language (IDL); helped with the structure design of EaR^{3}T; and helped with interpreting the results and writing the paper. SM helped with the OCO-2 data interpretation. VN trained and provided the CNN model. MN helped with the SPN-S instrument calibration and data processing. JG and GF helped with testing EaR^{3}T and the LES data interpretation. RH provided the AHI data and helped with the data interpretation. HI helped with the implementation of MCARaTS into EaR^{3}T.

References

Anderson, G. P., Clough, S. A., Kneizys, F. X., Chetwynd, J. H., and Shettle, E. P.: AFGL atmospheric constituent profiles (0–120 km), Tech. Rep. AFGL-TR-86–0110, Air Force Geophys. Lab., Hanscom Air Force Base, Bedford, Massachusetts, U.S.A., 1986.

Barker, H. and Liu, D.: Inferring optical depth of broken clouds from Landsat data, J. Climate, 8, 2620–2630, 1995.

Barker, H. W., Jerg, M. P., Wehr, T., Kato, S., Donovan, D. P., and Hogan, R. J.: A 3D cloud construction algorithm for the EarthCARE satellite mission, Q. J. Roy. Meteor. Soc., 137, 1042– 1058, https://doi.org/10.1002/qj.824, 2011.

Barker, H. W., Kato, S., and Wehr, T.: Computation of solar radiative fluxes by 1-D and 3-D methods using cloudy atmospheres inferred from A-train satellite data, Surv. Geophys., 33, 657–676, 2012.

Cahalan, R., Oreopoulos, L., Marshak, A., Evans, F., Davis, A., Pincus, R., Yetzen, K. H., Mayer, B., Yetzer, K. H., Mayer, B., Davies, R., Ackerman, T. P., Barker, H. W., Clothiaux, E. E., Ellingson, R. G., Garay, M. J., Kassianov, E., Kinne, S., Macke, A., O'Hirok, W., Partain, P. T., Prigarin, S. M., Rublev, A. N., Stephens, G. L., Szczap, F., Takara, E. E., Varnai, T., Wen, G., and Zhuravleva, T.: The I3RC: Bringing Together the Most Advanced Radiative Transfer Tools for Cloudy Atmospheres, B. Am. Meteorol. Soc., 86, 1275–1293, 2005.

Chen, H. and Schmidt, S.: er3t-v0.1.0, https://doi.org/10.5281/zenodo.7374196, 2022.

Chen, H., Schmidt, S., and Holz, R. E.: Synchronized Flight Videos for NASA CAMP[2]Ex, https://doi.org/10.5281/zenodo.7358509, 2022.

Crisp, D.: Measuring Atmospheric Carbon Dioxide from Space with the Orbiting Carbon Observatory-2 (OCO-2), P. Soc. Photo.-Opt. Ins., 9607, 960702, https://doi.org/10.1117/12.2187291, 2015.

Coddington, O., Schmidt, K. S., Pilewskie, P., Gore, W. J., Bergstrom, R., Roman, M., Redemann, J., Russell, P. B., Liu, J., and Schaaf, C. C.: Aircraft measurements of spectral surface albedo and its consistency with ground-based and space-borne observations, J. Geophys. Res., 113, D17209, doi:10.1029/2008JD010089, 2008.

Deneke, H., Barrientos-Velasco, C., Bley, S., Hünerbein, A., Lenk, S., Macke, A., Meirink, J. F., Schroedter-Homscheidt, M., Senf, F., Wang, P., Werner, F., and Witthuhn, J.: Increasing the spatial resolution of cloud property retrievals from Meteosat SEVIRI by use of its high-

resolution visible channel: implementation and examples, Atmos. Meas. Tech., 14, 5107–5126, https://doi.org/10.5194/amt-14-5107-2021, 2021.

Deutschmann, T., Beirle, S., Friess, U., Grzegorski, M., Kern, C., Kritten, L., Platt, U., Prados-Roman, C., Pukite, J., Wagner, T., Werner, B., and Pfeilsticker, K.: The Monte Carlo atmospheric radiative transfer model McArtim: introduction and validation of Jacobians and 3-D features, J. Quant. Spectrosc. Ra., 112(6), 1119–1137, ISSN 0022-4073, doi:10.1016/j.jqsrt.2010.12.009, 2011.

Doicu, A., Efremenko, D., and Trautmann, T.: A multi-dimensional vector spherical harmonics discrete ordinate method for atmospheric radiative transfer, J. Quant. Spectrosc. Ra., 118, 121–131, https://doi.org/10.1016/j.jqsrt.2012.12.009, 2013.

Emde, C., Barlakas, V., Cornet, C., Evans, F., Korkin, S., Ota, Y., Labonnote, L. C., Lyapustin, A., Macke, A., Mayer, B., and Wendisch, M.: IPRT polarized radiative transfer model intercomparison project – Phase A, Journal of Quantitative Spectroscopy and Radiative Transfer, 164, 8–36, https://doi.org/10.1016/j.jqsrt.2015.05.007, 2015.

Emde, C., Buras-Schnell, R., Kylling, A., Mayer, B., Gasteiger, J., Hamann, U., Kylling, J., Richter, B., Pause, C., Dowling, T., and Bugliaro, L.: The libRadtran software package for radiative transfer calculations (version 2.0.1), Geosci. Model Dev., 9, 1647–1672, https://doi.org/10.5194/gmd-9-1647-2016, 2016.

Evans, K. F.: The spherical harmonics discrete ordinate method for three-dimensional atmospheric radiative transfer, J. Atmos. Sci., 55, 429–446, 1998.

Gatebe, C. K., Jethva, H., Gautam, R., Poudyal, R., and Várnai, T.: A new measurement approach for validating satellite-based above-cloud aerosol optical depth, Atmos. Meas. Tech., 14, 1405–1423, https://doi.org/10.5194/amt-14-1405-2021, 2021.

Gristey, J. J., Feingold, G., Glenn, I. B., Schmidt, K. S., and Chen, H.: Surface Solar Irradiance in Continental Shallow Cumulus Fields: Observations and Large-Eddy Simulation, J. Atmos. Sci., 77, 1065–1080, https://doi.org/10.1175/JAS-D-19-0261.1, 2020a.

Gristey, J. J., Feingold, G., Glenn, I. B., Schmidt, K. S., and Chen, H.: On the Relationship Between Shallow Cumulus Cloud Field Properties and Surface Solar Irradiance, Geophysical Research Letters, 47, e2020GL090152, https://doi.org/10.1029/2020GL090152, 2020b.

Gristey, J. J., Feingold, G., Glenn, I. B., Schmidt, K. S., and Chen, H.: Influence of Aerosol Embedded in Shallow Cumulus Cloud Fields on the Surface Solar

Irradiance, Journal of Geophysical Research: Atmospheres, 127, e2022JD036822, https://doi.org/10.1029/2022JD036822, 2022.

Heidinger, A. K., Foster, M. J., Walther, A., and Zhao, X.: The Pathfinder Atmospheres-Extended AVHRR climate dataset, B. Am. Meteorol. Soc., 95, 909–922, https://doi.org/10.1175/BAMS-D-12-00246.1, 2014.

Illingworth, A. J., Barker, H. W., Beljaars, A., Chepfer, H., Delanoe, J., Domenech, C., Donovan, D. P., Fukuda, S., Hirakata, M., Hogan, R. J., Huenerbein, A., Kollias, P., Kubota, T., Nakajima, T., Nakajima, T. Y., Nishizawa, T., Ohno, Y., Okamoto, H., Oki, R., Sato, K., Satoh, M., Wandinger, U., Wehr, T., and van Zadelhoff, G.: The EarthCARE Satellite: the next step forward in global measurements of clouds, aerosols, precipitation and radiation, B. Am. Meteorol. Soc, 96, 1311–1332, https://doi.org/10.1175/BAMS-D-12-00227.1, 2015.

Iwabuchi, H.: Efficient Monte Carlo methods for radiative transfer modeling, J. Atmos. Sci., 63, 2324–2339, 2006.

Kindel, B. C., Schmidt, K. S., Pilewskie, P., Baum, B. A., Yang, P., and Platnick, S.: Observations and modeling of ice cloud shortwave spectral albedo during the Tropical Composition, Cloud and Climate Coupling Experiment (TC^4), J. Geophys. Res., 115, D00J18, doi:10.1029/2009JD013127, 2010.

King, M., and Platnick, S.: The Earth Observing System (EOS), Comprehensive Remote Sensing, 7, 26, doi:10.1016/b978-0-12-409548-9.10312-4, 2018.

Levis, A., Schechner, Y. Y., Davis, A. B., and Loveridge, J.: Multi-View Polarimetric Scattering Cloud Tomography and Retrieval of Droplet Size, Remote Sens., 12, 2831, https://doi.org/10.3390/rs12172831, 2020.

Li, J., Scinocca, J., Lazare, M., McFarlane, N., von Salzen, K., and Solheim, L.: Ocean Surface Albedo and Its Impact on Radiation Balance in Climate Models, J. Climate, 19, 6314–6333, 2006.

Long, C. N., Bucholtz, A., Jonsson, H., Schmid, B., Vogelmann, A., and Wood, J.: A Method of Correcting for Tilt from Horizontal in Downwelling Shortwave Irradiance Measurements on Moving Platforms, The Open Atmospheric Science Journal, 4, 78–87, 2010.

Loveridge, J., Levis, A., Di Girolamo, L., Holodovsky, V., Forster, L., Davis, A. B., and Schechner, Y. Y.: Retrieving 3D distributions of atmospheric particles using Atmospheric Tomography with 3D Radiative Transfer – Part 1: Model description and Jacobian calculation, Atmos.

Meas. Tech. Discuss. [preprint], https://doi.org/10.5194/amt-2022-251, in review, 2022.

Masuda, R., Iwabuchi, H., Schmidt, K. S., Damiani, A. and Kudo, R.: Retrieval of Cloud Optical Thickness from Sky-View Camera Images using a Deep Convolutional Neural Network based on Three-Dimensional Radiative Transfer, Remote Sensing, 11(17), 1962, doi:10.3390/rs11171962, 2019.

Marshak, A., Davis, A., Wiscombe, W., and Cahalan, R.: Radiative smoothing in fractal clouds, J. Geophys. Res., 100, 26247–26261, https://doi.org/10.1029/95JD02895, 1995.

Marshak, A., Wen, G., Coakley, J., Remer, L., Loeb, N. G., and Cahalan, R. F.: A simple model for the cloud adjacency effect and the apparent bluing of aerosols near clouds, J. Geophys. Res., 113, D14S17, https://doi.org/10.1029/2007JD009196, 2008.

Massie, S. T., Schmidt, K. S., Eldering, A., and Crisp, D.: Observational evidence of 3-D cloud effects in OCO-2 CO_2 retrievals, J. Geophys. Res. Atmos., 122, 7064–7085, https://doi.org/10.1002/2016JD026111, 2017.

Mayer, B. and Kylling, A.: Technical note: The libRadtran software package for radiative transfer calculations – description and examples of use, Atmos. Chem. Phys., 5, 1855–1877, https://doi.org/10.5194/acp-5-1855-2005, 2005.

Mayer, B.: Radiative transfer in the cloudy atmosphere, EPJ Web of Conferences, 1, 75–99, doi:10.1140/epjconf/e2009-00912-1, 2009.

Mlawer, E. J., Taubman, S. J., Brown, P. D., Iacono, M. J., and Clough, S. A.: Radiative transfer for inhomogeneous atmospheres: RRTM, a validated correlated-k model for the longwave, J. Geophys. Res., 102, 16663–16682, 1997.

Nakajima, T. and King, M. D.: Determination of the optical thickness and effective particle radius of clouds from reflected solar radiation measurements. Part I: Theory, J. Atmos. Sci., 47, 1878–1893, 1990.

Nataraja, V., Schmidt, S., Chen, H., Yamaguchi, T., Kazil, J., Feingold, G., Wolf, K., and Iwabuchi, H.: Segmentation-Based Multi-Pixel Cloud Optical Thickness Retrieval Using a Convolutional Neural Network, Atmos. Meas. Tech., 15, 5181–5205, doi:10.5194/amt-15-5181-2022, 2022.

Norgren, M. S., Wood, J., Schmidt, K. S., van Diedenhoven, B., Stamnes, S. A., Ziemba, L. D., Crosbie, E. C., Shook, M. A., Kittelman, A. S., LeBlanc, S. E., Broccardo, S., Freitag, S., and Reid, J. S.: Above-aircraft cirrus cloud and aerosol optical depth from hyperspectral

irradiances measured by a total-diffuse radiometer, Atmos. Meas. Tech., 15, 1373–1394, https://doi.org/10.5194/amt-15-1373-2022, 2022.

Payne, V. H., Drouin, B. J., Oyafuso, F., Kuai, L., Fisher, B. M., Sung, K., Nemchicka, D., Crawford, T. J., Smyth, M., Crisp, D., Adkins, E., Hodges, J. T., Long, D. A., Mlawer, E. J., Merrelli, A., Lunny, E., and O'Dell, C. W.: Absorption coefficient (ABSCO) tables for the Orbiting Carbon Observatories: version 5.1, J. Quant. Spectrosc. Ra., 255, 1–16, https://doi.org/10.1016/j.jqsrt.2020.107217, 2020.

Pilewskie, P., Pommier, J., Bergstrom, R., Gore, W., Howard, S., Rabbette, M., Schmid, B., Hobbs, P. V., and Tsay, S. C.: Solar spectral radiative forcing during the Southern African Regional Science Initiative, J. Geophys. Res., 108, 8486, https://doi.org/10.1029/2002JD002411, 2003.

Pincus, R. and Evans, K. F.: Computational cost and accuracy in calculating three-dimensional radiative transfer: Results for new implementations of Monte Carlo and SHDOM, J. Atmos. Sci., 66, 3131–3146, 2009.

Platnick, S., King, M. D., Ackerman, S. A., Menzel, W. P., Baum, B. A., Riédi, J. C., and Frey, R. A.: The MODIS cloud products: Algorithms and examples from Terra, IEEE T. Geosci. Remote, 41, 459–473, 2003.

Reid, J. S., Maring, H. B., Narisma, G., van den Heever, S., DiGirolamo, L., Ferrare, R., Lawson, P., Mace, G. G., Simpas, J., Tanelli, S., Ziemba, L., van Diedenhoven, B., Bruintjes, R., Bucholtz, A., Cairns, B., Cambaliza, M. O., Chen, G., Diskin, G. S., Flynn, J. H., Hostetler, C. A., Holz, R. E., Lang, T. J., Schmidt, K. S., Smith, G., Sorooshian, A., Thompson, E. J., Thornhill, K. L., Trepte, C., Wang, J., Woods, S., Yoon, S., Alexandrov, M., Alverez, S., Amiot, C., Bennett, J. R., Brooks, M., Burton, S. P., Cayanan, E., Chen, H., Collow, A., Crosbie, E., DaSilva, A., DiGangi, J. P., Flagg, D. D., Freeman, S. W., Fu, D., Fukada, E., Hilario, M. R. A., Hong, Y., Hristova-Veleva, S. M., Kuehn, R., Kowch, R. S., Leung, G. R., Loveridge, J., Meyer, K., Miller, R., Montes, M. J., Moum, J. N., Nenes, T., Nesbit, S. W., Norgen, M., Novak, E., Rauber, R. M., Reid, E. A., Rutledge, S., Schlosser, J. S., Sekiyama, T. T., Shook, M. A., Sokolowsky, G. A., Stamnes, S. A., Sy, O. O., Tanaka, T. Y., Wasilewski, A., Xian, P., Xiao, Q., and Zavaleta, J.: The coupling between tropical meteorology, aerosol lifecycle, convection, and radiation, during the Clouds, Aerosol and Monsoon Processes Philippines Experiment (CAMP^{2}Ex), B. Am. Meteorol. Soc., *in review*, 2022.

Ronneberger, O., Fischer, P., and Brox, T.: U-net: Convolutional networks for biomedical image

1456   segmentation, in: International Conference on Medical image computing and computer-
1457   assisted intervention, 234–241, Springer, https://doi.org/10.1007/978-3- 319-24574-4_28,
1458   2015.
1459   Rothman, L., Jacquemart, D., Barbe, A., Chris Benner, D., Birk, M., Brown, L., Carleer, M.,
1460   Chackerian, C., Chance, K., Coudert, L., Dana, V., Devi, V., Flaud, J.-M., Gamache, R.,
1461   Gold- man, A., Hartmann, J.-M., Jucks, K., Maki, A., Mandin, J.- Y., Massie, S., Orphal, J.,
1462   Perrin, A., Rinsland, C., Smith, M., Tennyson, J., Tolchenov, R., Toth, R., Vander Auwera,
1463   J., Varanasi, P., and Wagner, G.: The HITRAN 2004 molecular spectroscopic database, J.
1464   Quant. Spectrosc. Ra., 96, 139–204, https://doi.org/10.1016/j.jqsrt.2004.10.008, 2005.
1465   Schmidt, K. S., Pilewskie, P., Platnick, S., Wind, G., Yang, P., and Wendisch, M.: Comparing
1466   irradiance fields derived from Moderate Resolution Imaging Spectroradiometer airborne
1467   simulator cirrus cloud retrievals with solar spectral flux radiometer measurements, J. Geophys.
1468   Res., 112, D24206, doi:10.1029/2007JD008711, 2007.
1469   Schmidt, S., Pilewskie, P., Mayer, B., Wendisch, M., Kindel, B., Platnick, S., King, M. D., Wind,
1470   G., Arnold, G. T., Tian, L., Heymsfield, G., and Kalesse, H.: Apparent absorption of solar
1471   spectral irradiance in heterogeneous ice clouds, J. Geophys. Res., 115, D00J22,
1472   https://doi.org/10.1029/2009JD013124, 2010.
1473   Schmidt, S., Massie, S., Chen, H., Crisp, D., Kulawik, S., Chen, Y.-W., Merrelli, A., McDuffie, J.,
1474   Iwabuchi, H.: Uncovering the Mechanism for Trace Gas Spectroscopy Biases in the Vicinity
1475   of Clouds With the OCO-2 3D Radiative Transfer Satellite Radiance Simulator, Atmos. Meas.
1476   Tech., *in prep.*, 2022.
1477   Song, S., Schmidt, K. S., Pilewskie, P., King, M. D., Heidinger, A. K., Walther, A., Iwabuchi, H.,
1478   Wind, G., and Coddington, O. M.: The Spectral Signature of Cloud Spatial Structure in
1479   Shortwave Irradiance, Atmos. Chem. Phys., 16, 13791–13806, https://doi.org/10.5194/acp-
1480   16-13791-2016, 2016.
1481   Spada, F., Krol, M. C., and Stammes, P.: McSCIA: application of the Equivalence Theorem in a
1482   Monte Carlo radiative transfer model for spherical shell atmospheres, Atmos. Chem. Phys.,
1483   6, 4823–4842, https://doi.org/10.5194/acp-6-4823-2006, 2006.
1484   Vermote, E. F., Roger, J. C., and Ray J. P.: MODIS Surface Reflectance User's Guide, MODIS
1485   Land Surface Reflectance Science Computing Facility, Version 1.4, 1-35, 2015.
1486   Wood, J., Smyth, T. J., and Estellés, V.: Autonomous marine hyperspectral radiometers for

1488   determining solar irradiances and aerosol optical properties, Atmos. Meas. Tech., 10, 1723–
1489   1737, https://doi.org/10.5194/amt-10-1723-2017, 2017.